UNIVERSITÀ DEGLI STUDI DI TRENTO
FACOLTÀ DI SCIENZE MATEMATICHE
FISICHE E NATURALI

Tesi di Dottorato di Ricerca in Fisica
Ph.D. Thesis in Physics

---

# Quantum Monte Carlo Methods applied to strongly correlated and highly inhomogeneous many–Fermion systems

Candidate:
**Lucia Dandrea**

Supervisor:
**Dr. Francesco Pederiva**

February 2009

To Pradiip

# Contents

**1 Introduction** **1**
- 1.1 Laterally confined 2D Electron Gas . . . . . . . . . . . . . . . . 2
- 1.2 Fermionic Shadow Wave Function . . . . . . . . . . . . . . . . . 6

**2 Quantum Monte Carlo Methods** **9**
- 2.1 Variational Monte Carlo . . . . . . . . . . . . . . . . . . . . . . . 9
  - 2.1.1 The Metropolis algorithm . . . . . . . . . . . . . . . . . . 10
- 2.2 Diffusion Monte Carlo . . . . . . . . . . . . . . . . . . . . . . . . 10
  - 2.2.1 Description of DMC method . . . . . . . . . . . . . . . . 11
  - 2.2.2 Importance sampling . . . . . . . . . . . . . . . . . . . . . 12
  - 2.2.3 Fixed–node approximation . . . . . . . . . . . . . . . . . . 13
  - 2.2.4 Technical details . . . . . . . . . . . . . . . . . . . . . . . 14
  - 2.2.5 Forward-walking algorithm . . . . . . . . . . . . . . . . . . 15

**3 Method details for the confined two dimensional electron gas** **17**
- 3.1 Hamiltonian . . . . . . . . . . . . . . . . . . . . . . . . . . . . . . 17
- 3.2 Trial wavefunction . . . . . . . . . . . . . . . . . . . . . . . . . . 18
  - 3.2.1 Optimization trial wavefunction . . . . . . . . . . . . . . . 19
- 3.3 Ewald Summation . . . . . . . . . . . . . . . . . . . . . . . . . . 21
  - 3.3.1 The procedure . . . . . . . . . . . . . . . . . . . . . . . . . 22
  - 3.3.2 Solution of Poisson equation for $\rho_2$ . . . . . . . . . . . . 24
  - 3.3.3 Solution of Poisson equation for $\rho_1$ . . . . . . . . . . . . 25
  - 3.3.4 Average potential in the cell equal to zero . . . . . . . . 25
  - 3.3.5 Computation of $\xi$ . . . . . . . . . . . . . . . . . . . . . . 26
  - 3.3.6 Implementation of Ewald Summation . . . . . . . . . . . 26
- 3.4 CHAMP . . . . . . . . . . . . . . . . . . . . . . . . . . . . . . . . 27
  - 3.4.1 Particularly noteworthy features of CHAMP . . . . . . . 27

**4 Ground state properties of the laterally confined 2D electron gas** **29**
  - 4.0.2 Results at $\hbar\omega_0 = 4$meV . . . . . . . . . . . . . . . . . . . 30
  - 4.0.3 Results at $\hbar\omega_0 = 2$meV and $\hbar\omega_0 = 6$meV . . . . . . . . . 36

4.1 Overview . . . . . . . . . . . . . . . . . . . . . . . . . . . . . 42

**5 Fermionic Shadow Wave Function 45**

5.1 Shadow Wave Function . . . . . . . . . . . . . . . . . . . . . . . . 45
5.2 Antisymmetric Shadow Wave Function . . . . . . . . . . . . . . 47
5.3 Fermionic Shadow Wave Function . . . . . . . . . . . . . . . . . 48
    5.3.1 FSWF problems . . . . . . . . . . . . . . . . . . . . . . . . 49
    5.3.2 Proposed solution to FSWF sign problem . . . . . . . . . 50
5.4 Ground state properties of $^3$He vacancies . . . . . . . . . . . . 51
    5.4.1 Technical details . . . . . . . . . . . . . . . . . . . . . . 51
    5.4.2 Results . . . . . . . . . . . . . . . . . . . . . . . . . . . 53

**6 Conclusions and perspectives 59**

**Acknowledgements 63**

**List of Figures 65**

**List of Tables 69**

**Bibliography 71**

# Chapter 1

# Introduction

The theoretical understanding of *many-body systems* is one of main challenges in quantum Physics. It is already impossible to solve a system with more than four particles using analytic methods. Theoretical physics has made many efforts in order to develop tools to study many-body systems. To overcome the limit of applicability of exact analytical solution it is necessary to use some approximations. An outstanding examples is given by Mean-field theory (MFT). The main idea of MFT is to replace all interactions to any one body with an average or effective interaction. This reduces any multi-body problem into an effective one-body problem. However one MFT limitation is that it is not possible to study systems with local dis-homogeneities, like solids.

Methods trying to compute on exact solution of Schroedinger equation for a given Hamiltonian $\hat{H}$ are much more demanding. For a limited number of particles ($N < 10$), it is possible to compute eingenvalues and eigenstates of $\hat{H}$ by computing its matrix elements on a given basis, and then diagonalizing the matrix. For larger system the direct knowledge of the wavefunction is not possible, and stochastic techniques, known under the names of (Quantum) Monte Carlo methods must be used.

There are many variants of QMC methods with different possible applications. In this work we focus on two types: Variational (VMC) and Diffusion (DMC) Monte Carlo methods. VMC and DMC are very used and tested methods. The scientific community knows very well their limits and capacities. These two methods are particularly indicated in order to study the ground state properties of a quantum system at temperature of 0K. However they can not give information on time evolution of the system.

In this work we studied two different kinds of systems. The first is a two–dimensional electron gas laterally confined by a harmonic potential in the effective mass–dielectric constant approximation. The second is a solid $^3$He in presence of defects.

We chose these systems not only for the physics interest but also for the computational challenge they pose.

First of all studying Fermion system by QMC methods means to face the notorious *sign problem*. In the first system, there is the classical sign problem of the DMC method, which can be milded in our case by a well known approximation, the *fixed–node* approximation. The second system requires a variational treatment in which we have a integral sign problem. Computing the mean value of the energy, using Fermionic Shadow Wave Functions (FSWF), positive and negative terms in the integral appear. Summing these terms, the positive contributions tends to cancel the negative ones. However the noise is too large to obtain a useful signal.

Furthermore the electrons system is confined, strongly correlated and we do not know the equilibrium phase a priori. All these aspects make difficult the computation. We also studied the equation state of $^3$He solid with a vacancy, meaning that the system is highly dis-homogeneous making it necessary to find a wavefunction which can describe a dis-homogeneous phase.

The effort of this work is to find a solution to some technical problem that you have when you want to study a strongly correlated and highly inhomogeneous many–Fermion systems with the Quantum Monte Carlo Methods. In this way we want to try to say more about these systems.

## 1.1 Laterally confined 2D Electron Gas

The two dimensional (2D) electron gas laterally confined by some potential is a fundamental model in many-body physics since the progress in nanostructure technology has allowed the fabrication of 2D quantum stripes.

There are many different kinds of objects that go under the name of quantum wires. Our interest is focused on semiconductor quantum wires.

It is possible to create a two-dimensional electron gas (2DEG) at junction interface of two semiconductor (see fig. 1.1). In particular, a kind of quantum wires

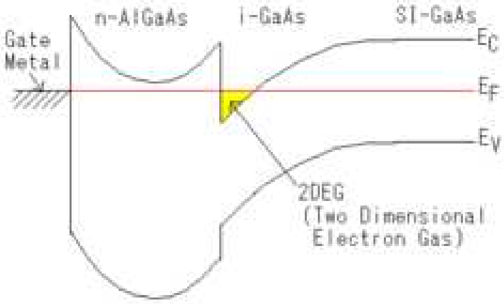

Figure 1.1: Energy Band of basic high-electron-mobility-transistors (HEMT).

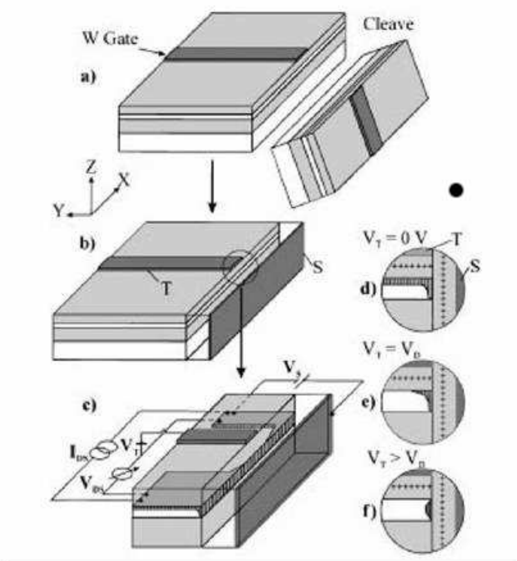

Figure 1.2: A one dimensional quantum wire realized at the edge of a two dimensional electron gas [1]

is obtained by etching a semiconductor quantum well, obtained at the junction between differently doped semiconductors (e.g. GaAs/AlGaAs) (see figure 1.2). Split-gates technique is a method for creating a smooth one-dimensional constriction in a 2DEG. When a negative voltage $V_g$ is applied to a lithographically defined pair of Schottky split-gates above a GaAs/$Al_xGa_{1-x}$As heterostructure, shown in Fig. 1.3, the 2DEG is depleted from beneath the gates and a 1D channel is left defined between them. If the elastic mean free path $l_e$ is much greater than the width W and length L of the channel, transport through the 1D constriction is ballistic and the differential conductance, $G(V_g)=N(2e^2/h)$, is quantized, where $N$ is the number of transmitted 1D subbands.

Experiments in these nanostructures have pointed out the quantization of the conductance $G$ in units of $2e^2/h$, which reflects the number of active channels in the transport measurements[4, 5, 6]. A conductance structure close to $G = 0.7(2e^2/h)$ has been observed in many cases[7, 8, 2, 3, 9, 10] (see figure 1.4). These experiments are made on quantum point contacts (which are quantum wires of length $l = 0$) or on quantum wires with length of few $\mu$m, formed in GaAs/$Al_xGa_{1-x}$As heterostructures, generally in the absence of a magnetic field. The intensity of this structure changes from $0.5(2e^2/h)$ to $0.7(2e^2/h)$, that depends on length of the quantum wire, electron density $n_{1D}$ and temperature.

This structure has given rise to many interpretations based on spontaneous spin polarization of the system mediated through the exchange-correlation interaction[11, 12, 13, 14, 15, 16], on possible manifestation of a Kondo effect[17,

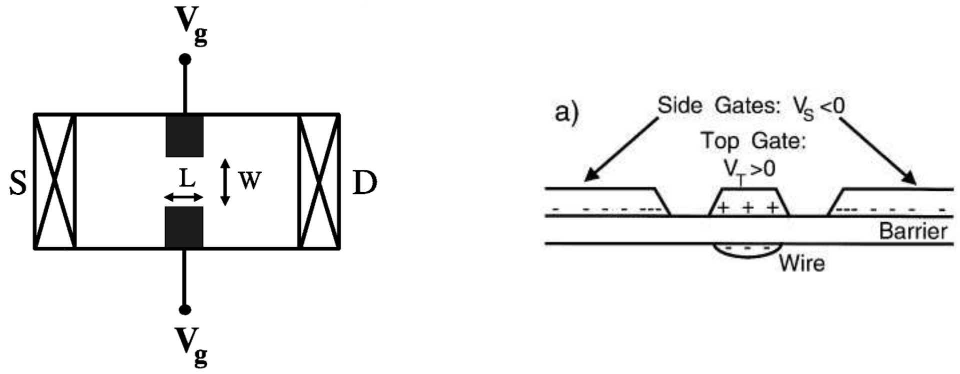

Figure 1.3: (left) Schematic of a split-gate device, where S and D represent the source and drain contacts [2]. (Right) Gate configuration used to define the wire. The top gate and side gates are separately adjusted to control the electron density and the wire confinement potential [3].

18, 19], or of Wigner crystallization of the confined electron gas at low density[20] or of a Tomonaga-Luttinger liquid behavior[21, 22, 23, 24, 25, 26, 27, 28, 29, 30]. All these results are based on specific models or approximations like, for example, the local spin density functional theory.

In this thesis we present a fixed node diffusion Monte Carlo calculation of the ground state of a 2D quantum stripe of infinite length and finite width described by the 2D Hamiltonian of $N$ interacting electrons laterally confined by a parabolic potential. The extension of the stripe in the third dimension is neglected, as in most theoretical descriptions. This approximation is justified by the fact that the confinement of the electron in the quantum well is extremely strong, and at all relevant densities only one subband is occupied. We calculate the ground state energy for the unpolarized and fully spin-polarized liquid phases and solid phase. Previous Monte Carlo calculations of quasi-unidimensional systems have been performed by Casula, Sorella, and Senatore [31]. The authors in that case considered a one dimensional system with an interaction that effectively includes the width of the wire. However, being the Hamiltonian one-dimensional, no phase transitions can occur in the system, according to the Lieb–Mattis theorem[32]. Our calculation being fully two–dimensional, makes it possible to discuss relative stability of phases with different symmetry.

We met many technical problems to implement this model.

First of all it was necessary write the Ewald summation for a confined two-dimensional system in order to describe the Coulomb potential. We found an expression for the Ewald sum that was not simple to implement. We had to tabulate all the terms to minimize the computational time. In one integral term we needed to find a specific numeric method in order to obtain a satisfactory

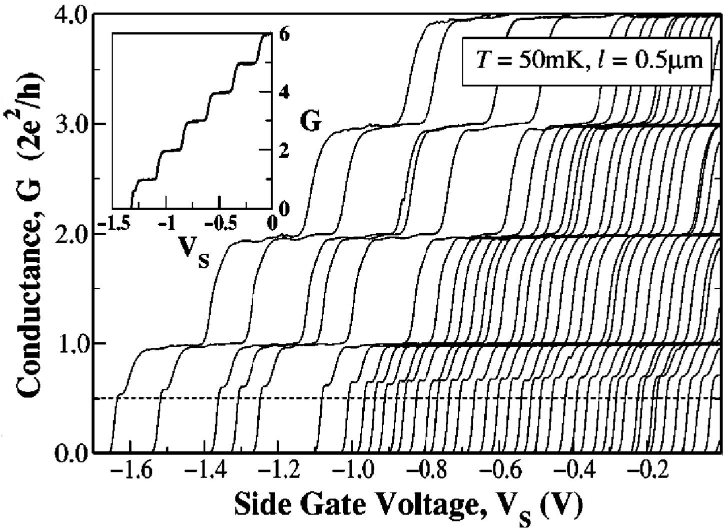

Figure 1.4: Experimental result[7]. Conductance of a $l = 0.5\mu$m quantum wire as a function of side gate voltage for $V_T$ =560 mV-1500 mV (right to left). Inset: Conductance as a function of side gate voltage for $V_T$=1.5 V

convergence. Then many tests were necessary to optimize the Ewald break up.

We made many checks on wavefunction and also we verified the ergodicity of the system was guaranteed.

We did not have a direct comparison with another computational model that could verify the correctness of our work. We made all the possible tests to assert our work could explain this confined two-dimensional electron system.

The system was studied as a function of $r_s$ ($0.5 \leq r_s \leq 7$) and $\hbar\omega_0$ ($\hbar\omega_0$ =2, 4, 6 meV). $\omega_0$ is the confining parameter and $r_s$ is the one–dimensional Wigner-Seitz parameter $r_s = 1/2\rho^{1D}$. The values of $r_s$ correspond at values of $\rho_{1D}$ in the range $10^4 - 10^6\text{cm}^{-1}$. The combination of $\omega_0$ with $\rho_{1D}$ reproduces the two–dimensional density of the experiments [7, 2, 3].

The results show us how the system tends to become more localized increasing the confining parameter $\omega_0$. In this range of $\omega_0$ for $r_s > 3$ we found the polarized phase has the lowest energy. This last observation is the most interest result of our work. This result could explain the conductance anomaly in experiments.

## 1.2 Fermionic Shadow Wave Function

The Fermionic Shadow Wave Function is an extension, for Fermion system, of Shadow Wave Functions (SWF)[33]. SWF is a particular class of many–body wave functions employed to study bosonic systems. Its main property is that it describes a disordered phase and/or a crystalline phase of a quantum system within the same functional form, which is manifestly translationally invariant. In this way, it is possible to study non–homogeneous systems and phase transitions. Using SWF, it is possible for example to study the equilibrium point between two different phases of the system, which naturally emerges from the wavefunction.

SWF were largely used to study properties of liquid–solid $^4$He [34] and $^3$He [35], system with phase coexistence [36] or presence of defects or impurities [37] and superfluid liquids with vortex excitations [38].

As it will be explained in the following chapters, the use of SWF for Fermions presents severe technical difficulties in some cases. In the thesis the first application of a FSWF antisymmetrized on the auxiliary degree of freedom is presented, in wich some relevant physical properties has been computed successfully.

The general form of FSWF would be useful to describe many–body systems with the coexistence of different phases as well in the presence of defects or impurities, but it requires overcoming a significant sign problem. As an application, we studied the energy to activate vacancies in solid $^3$He.

$^3$He is a very strongly interacting quantum system. In figure 1.5 the $^3$He phase diagram is represented. Experimentally one finds that for temperatures in the mK region, two superfluid phases appear in the liquid, and a quasi-antiferromagnetic ordered bcc phase shows up in the solid, which changes into a normal antiferromagnetic when the magnetic field is increased.

We focus our attention on the solid phase. In VMC or DMC the solid phase is generally described by product of Gaussian orbitals. For a Fermion system it is necessary, in principle, to use a determinant of Gaussians in order to consider the antisymmetry of the system. In a regime of strong localization the determinant of Gaussians is essentially equivalent to a product of localized orbitals because of the rare occurrence of exchange among particles on different lattice sites. For this reason, the simulation of a homogeneous quantum crystal, even in presence of the Pauli principle, does not represent a significant challenge.

When the lattice symmetry is locally broken by the presence of the vacancy, exchange among the atoms in the crystal becomes much more effective. The phenomenon can also be viewed as a “motion” of the vacancy through the crystal itself. The effect due to the Fermion nature of $^3$He become then evident at the level of wavefunction. However, even a Slater determinant of localized orbitals would not be a satisfactory choice. In fact, the relaxation of the lattice structure around the vacancy contributes for a large fraction to the vacancy formation

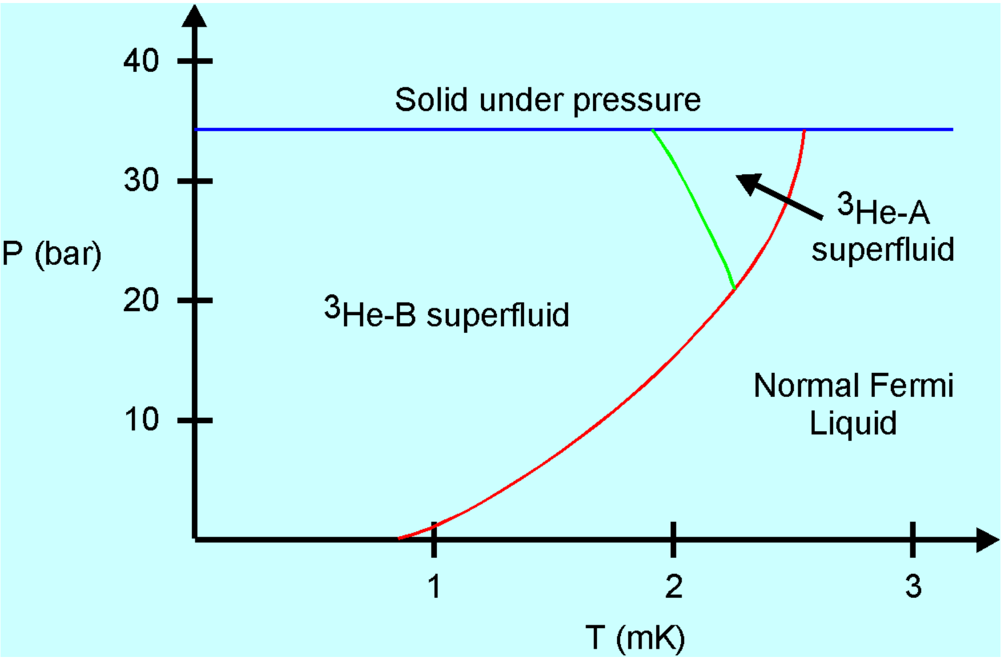

Figure 1.5: Phase diagram of $^3$He below 3 mK. The solid phase appears only above the pressure of 34 bar. At high temperatures the liquid is in the normal Fermi state. There are two superfluid phases, A and B.

energy. FSWF is the only wavefunction that can account for all these characters of the system.

Our goal was find a way to make the calculations feasible. For solid $^3$He with vacancies the improvements we have developed allowed us to meet this challenge.

# Chapter 2

# Quantum Monte Carlo Methods

The *Monte Carlo methods* [39] are a set of algorithms, which use the random (or pseudo–random) numbers in order to solve mathematical problems. The Monte Carlo methods are mainly used to compute integrals. The main difficulty in solving an integral with the standard methods is the computation effort increases exponentially with dimensionality of the integration domain. MC avoids this problem. In fact the evaluation of a multidimensional integral is made by sampling the integrand and averaging the sampled values. The statistical error in the value of integral decreases as the square root of the number of sampling points used, regardless of dimensionality. This is a consequence of the *central limit theorem.*

In particular we are interested to introduce the *Quantum Monte Carlo Method* (QMC) for study quantistic system. We start introducing the *Variational Monte Carlo* (VMC) and the *Diffusion Monte Carlo* (DMC) method. In chapter 5 we talk about the *Fermionic Shadow wave function* FSWF, which are a special way to do VMC.

## 2.1 Variational Monte Carlo

The Variational Monte Carlo (VMC) method is based on variational principle. The expectation value of $\hat{H}$ evaluated with a trial wavefunction $\psi_T$ provides a rigorous upper bound on the exact ground-state energy $E_0$:

$$E_V = \frac{\int \psi_T^*(R)\hat{H}\psi_T(R)dR}{\int \psi_T^*(R)\psi_T(R)dR} \geq E_0 \tag{2.1}$$

where $R = (\vec{r}_1, \vec{r}_2, ..., \vec{r}_N)$ is the $3N$-dimensional vector and $\vec{r}_i$ is the position of the $i$-th particle. In a VMC simulation the energy $E_V$ is evaluated using the

Metropolis algorithm [40] and the integral 2.1 is rewritten in this way:

$$E_V = \frac{\int |\psi_T(R)|^2 \left[\psi_T(R)^{-1}\hat{H}\psi_T(R)\right] dR}{\int |\psi_T(R)|^2 dR} \tag{2.2}$$

where $|\psi_T(R)|^2$ becomes the probability density and $\psi_T(R)^{-1}\hat{H}\psi_T(R)$ is the quantity to accumulate. In VMC the configurations $R$ are sampled following a distribution probability.

VMC is often used to optimize trial wavefunction.

### 2.1.1 The Metropolis algorithm

The *Metropolis algorithm* (M(RT)$^2$) has the great advantage of allowing an arbitrarily complex distribution to be sampled in a straightforward way, without knowledge of its normalization.

Suppose we define a $3N-$ dimensional vector $R$, a particular value of $R$ is called a *walker* or *configuration.* The probability density of finding the system in the configuration $R$ will be denoted by $P(R)$ (where $P(R) \geq 0$ and $\int P(R)dR = 1$). The M(RT)$^2$ generated the sequence of sampling points $R_m$ by moving the single walker according the following rules [41]:

1) Start the walker at a random position $R$.

2) Make a trial move to a new position $R'$ chosen from some probability density function $T(R' \leftarrow R)$.

3) Accept the trial move with probability

$$A(R' \leftarrow R) = Min\left(1, \frac{T(R \leftarrow R')P(R')}{T(R' \leftarrow R)P(R)}\right)$$

   If the trial move is accepted, the point $R'$ becomes the next point on the walk, otherwise the next point remains $R$.

4) Return to step 2 and repeat.

## 2.2 Diffusion Monte Carlo

A practical method of studying the properties of a many body quantum system is the Diffusion Monte Carlo (DMC) algorithm. DMC is a stochastic algorithm based on transforming the analytic continuation of the Schrödinger equation in imaginary time into a diffusion equation.

In this work we studied a system which is described by a real wavefunction, so we limit our explanation to the case of using a real wavefunction.

### 2.2.1 Description of DMC method

The Schrödinger equation in imaginary time $\tau = it$ is given by

$$-\frac{\partial}{\partial\tau}\psi(R,\tau) = H\psi(R,\tau) \tag{2.3}$$

A formal solution written in integral form is

$$\psi(R,\tau) = \int G(R,R',\tau)\psi(R',0)dR' \tag{2.4}$$

where the kernel $G(R,R',\tau)$ is the Green's function of the operator $H + \frac{\partial}{\partial\tau}$, and it can be expressed as the matrix element

$$G(R,R',\tau) = \langle R|e^{-(H-E_0)\tau}|R'\rangle = \sum e^{-(E_n-E_O)\tau}\phi_n^*(R)\phi_n(R') \tag{2.5}$$

where $\phi_n$ is a complete set of eigenvectors of $H$.
One starts choosing a *trial wavefunction* $\psi_T$, which is not orthogonal to the ground state of the system. It is possible to write $\psi_T$ as a linear combination of $\phi_n$:

$$\psi_T(R) = c_n\phi_n(R) \tag{2.6}$$

The evolution in imaginary time of $\psi_T$ is:

$$\psi_T(R,\tau) = e^{-(H-E_0)\tau}\psi(R,0) = e^{-(H-E_0)\tau}c_n\phi_n(R) \tag{2.7}$$

Considering the limit for $\tau \to \infty$ you obtain the ground state.

#### The non-interacting Hamiltonian

Let us consider the non interacting Hamiltonian of $N$ particles with mass $m$

$$H_0 = -\sum_i \frac{\hbar^2}{2m}\nabla_i^2 \tag{2.8}$$

the corresponding kernel $G_0$ is a Gaussian with variance proportional to $\sqrt{\tau}$:

$$G_0(R,R',\tau) = \left(\frac{m}{2\pi\hbar^2\tau}\right)^{\frac{3}{2}N} e^{-\frac{m(R-R')^2}{2\hbar^2\tau}} \tag{2.9}$$

this equation describes the Brownian diffusion of $N$ particles.
It possible to implement this equation writing the wavefunction as a set of discrete sampling points, the *walkers*:

$$|\psi(R)\rangle = \sum_k \langle x_k|\psi\rangle\,|x_k\rangle \tag{2.10}$$

where $|x_k\rangle = \delta(R - R_k)$ is eingenfunction of position.
The evolution in imaginary time step $\Delta\tau$ is:

$$\psi(R, \tau + \Delta\tau) = \sum_k G(R, R_k, \tau + \Delta\tau) \tag{2.11}$$

This set of Gaussian functions represents a distributions of *walkers*. In the limit of $\tau \to \infty$ these points represent the ground state of $H_0$.

### The interacting Hamiltonian

In order to solve the equation 2.3 with the Hamiltonian:

$$H = -\sum_i \frac{\hbar^2}{2m}\nabla_i^2 + V(R) \tag{2.12}$$

it is necessary to use the Trotter formula in this way:

$$G(R, R', \Delta\tau) \approx e^{-\left(\frac{V(R)+V(R')}{2} - E_T\right)\Delta\tau} G_0(R, R', \Delta\tau) \tag{2.13}$$

that introduces an error in $\Delta\tau$ ($O(\Delta\tau^3)$).
Now the kinetic term is separated from the potential term and the wavefunction can be rewritten

$$\psi(R, \tau + \Delta\tau) = \left(\frac{m}{2\pi\hbar^2\tau}\right)^{\frac{3}{2}N} \int e^{-\frac{m(R-R')^2}{2\hbar^2\tau}} e^{-\left(\frac{V(R)+V(R')}{2} - E_T\right)\Delta\tau} \psi(R', \tau) dR' \tag{2.14}$$

The kinetic part gives a diffusion term, the potential part gives a *branching* term:

$$w = e^{-\left(\frac{V(R)+V(R')}{2} - E_T\right)\Delta\tau} \tag{2.15}$$

$w$ represents a weight of the Green's function.
The integral 2.14 is solved with Monte Carlo method by propagating the particles according the diffusion term. Instead the branching term gives the probability of multiply a configuration at the next step.

## 2.2.2 Importance sampling

Solving equation 2.3 by a purely diffusive random-walk process with branching is rather inefficient, because the weight term 2.15 could have large fluctuations. For example, if $V(R)$ is the electron-electron and electron-ion Coulomb potential the branching term can diverge $\pm\infty$. This leads to a large fluctuations in the number of walkers and to a slow convergence when calculating averages [42].

One can overcome these difficulties by carrying out an *importance-sampling transformations* using a “trial” or “guiding” wavefunction $\psi_T(R)$ (Grimm and

Storer,1971; Ceperley and Kalos, 1979; Reynolds *et al.*, 1982). The idea is to multiply the both member of eq. 2.3 for a known $\psi_T(R)$ and rewrite it in terms of a new probability distribution $f(R,\tau) = \psi_T(R)\psi(R,\tau)$. After rearranging terms we obtain

$$-\frac{\partial f(R,\tau)}{\partial \tau} = -D\nabla^2 f(R,\tau) + (E_L(R) - E_T)f(R,\tau) + D\nabla \cdot (f(R,\tau)F_Q(R)) \tag{2.16}$$

where $D = \hbar^2/2m$. Here the "*quantum force*" $F_Q(R)$ is defined as:

$$F_Q(R) = \nabla ln|\psi_T(R)|^2 = 2\frac{\nabla\psi_T(R)}{\psi_T(R)}$$

and in the coefficient of the branching term $E_L$ is the *local energy* defined as:

$$E_L = \frac{\hat{H}\psi_T(R)}{\psi_T(R)}$$

Under the assumption that $\psi_T$ is not orthogonal to the ground state $\phi_0$, in the limit of $\tau \to \infty$ the distribution $f(R,\tau)$ becomes proportional to $\psi_T(R)\psi_0(R)$.

The three terms on the left-hand side of equation 2.16 represent a diffusion, drift and branching process respectively. An approximate Green's function for small time-step $\Delta\tau$ of such equation is given by the product of the individual diffusion, drift and branching Green's function[42]:

$$\begin{aligned} \tilde{G}(R', R, \Delta\tau) &= \left(\frac{m}{4D\pi\Delta\tau}\right)^{\frac{3N}{2}} \int dR" e^{\left[-\frac{(R'-R")^2}{4D\Delta\tau}\right]} \\ &\times \ \delta(R" - R - DF_Q(R)\Delta\tau) \\ &\times \ exp\left\{-\Delta\tau\left(\frac{1}{2}\left[E_L(R) + E_L(R')\right] - E_T\right)\right\} \end{aligned} \tag{2.17}$$

### 2.2.3 Fixed–node approximation

In the DMC algorithm the wavefunction $\psi(R)$ is represented by a population density, therefore the algorithm is well defined only if $\psi(R)$ is defined positive. $\psi(R)$ may also be everywhere negative, since the overall phase of the wavefunction is arbitrary. This implies that a wavefunction has to be without nodes. This is a problem if we are interested in Fermionic system. The *Fixed-node* approximation [42, 41] is a method for dealing with the fermion antisymmetry. Although not exact, it gives ground-state energies that can be proved to be an upper bound of the true ground state, which is always lower than the variational upper bound given by the wavefunction used to impose the nodal surface.

To apply the Fixed-node method the ground-state wavefunction have to be real and hence works only in systems with time reversal symmetry. A Fermionic wavefunction has a nodal structure that divides the space in many positive and negative pockets. The Fixed-node approximation consists in keeping the walkers in the pockets with the same sign. One scatters DMC walkers throughout the configuration space and moves them in the usually way. After every DMC move the sign of the trial wavefunction is checked. If the walker has crossed the trial nodal surface it is deleted or the move is rejected if an acceptance-rejection scheme is used.

If the nodes of the trial wavefunction are exact the result is the exact ground-state energy, otherwise an upper bound of the ground state energy of the Fermions is obtained. The challenge of a Fixed-node DMC calculation is find a trial wavefunction which has a nodal structure as close as possible to the real nodal structure. Finding a good nodal structure is necessary in order to minimize the *nodal-error*.

### 2.2.4 Technical details

In DMC calculation many technical details have to be considered.

#### Time step error

Developing DMC method is necessary to separate in the propagator the kinetic terms from potential term using Trotter formula (see Eq. 2.13). This step introduce a *time step error*. In order to evaluate this error it is necessary repeat the same calculation with different value of $\Delta\tau$. The best value is the extrapolation at $\Delta\tau = 0$.

#### Population bias

In DMC the population is a set of walkers. The number of walkers change during the computation due to the branching. In order to avoid wide fluctuations of population the weight may be corrected in this way:

$$w = \frac{N_0}{N} exp\left(-\Delta\tau(E_L - E_0)\right) \tag{2.18}$$

where $N$ is the number of walker and $N_0$ is the prefixed number of walker.

This correction allows to controll the population, but that modifies the sampling so it introduces a population error. Therefore it is necessary extrapolate the energy value in function of $1/N$ for high value of $N$.

#### Mixed estimator

In order to evaluate a generic operators $O(R)$, which do not commute with the Hamiltonian, it is necessary make a linear combination between VMC and DMC result. The mixed estimator consists in taking twice DMC result minus VMC result, in this way you obtain the mean value of $O(R)$ on the ground state:

$$\langle O\rangle = 2\,\langle\phi_0|O|\psi_T\rangle - \langle\psi_T|O|\psi_T\rangle + \vartheta(\alpha^2) \tag{2.19}$$

The bias affecting such estimate is of the second order in $\alpha$, where $\alpha$ is defined by $\phi_0 = \psi_T + \alpha\psi_\alpha$.

### 2.2.5 Forward-walking algorithm

An other method to evaluate operators, which do not commute with the Hamiltonian, is the Forward-walking [43, 44] algorithm.

The pure estimator of an operator $O(R)$ may be written as:

$$\langle O(\mathbf{R})\rangle = \frac{\left\langle \phi_0 \left| O(\mathbf{R})\frac{\phi_0}{\psi_T} \right| \psi_T \right\rangle}{\left\langle \phi_0 \left| \frac{\phi_0}{\psi_T} \right| \psi_T \right\rangle} \tag{2.20}$$

$\phi_0(\mathbf{R})/\psi_T(\mathbf{R})$ can be obtained from the asymptotic offspring of the $\mathbf{R}$ walker. The idea is to assign to each walker $\mathbf{R}_i$ a weight $W(\mathbf{R}_i)$ proportional to its number of descendants, $W(\mathbf{R}_i) = n(\mathbf{R}, \tau \to \infty)$. Eq. 2.20 becomes:

$$\langle O(\mathbf{R})\rangle = \frac{\sum_i O(\mathbf{R})W(\mathbf{R}_i)}{\sum_i W(\mathbf{R}_i)} \tag{2.21}$$

where the summation runs over all walkers and all times in the asymptotic regime.

# Chapter 3

# Method details for the confined two dimensional electron gas

## 3.1 Hamiltonian

In order to determine the Hamiltonian of the system we start from a two dimensional electron gas of density $\rho^{2D} = 1/\pi a^2$ in the effective mass-dielectric constant approximations. In this thesis we will consider effective units, assuming $\epsilon = 1$ and $m^* = 1$. The density of the gas is parametrized by the effective Wigner-Seitz radius in effective atomic units $r_s^{2D} = a/a_0^*$. For reasons of convenience, in the simulations we prefer to rescale all lengths in terms of a one-dimensional Wigner-Seitz parameter $r_s = L/2N$ where $N$ is the number of electrons, and $L$ is the length of the wire, which by this scaling depends only on the number of electrons, and not on the density. The one– and two–dimensional densities are related to each other as $\rho^{1D} = \rho^{2D} w(\rho^{1D})$, where $w$ is an estimate of the width of the wire. A possible definition of $w(r_s)$ is given by twice the distance from the center of the wire at which the transverse density decays to one half of the value at the center. Similarly we can relate $r_s^{2D}$ and $r_s$ as $r_s^{2D} \sim \sqrt{2r_s w(r_s)/\pi}$. With this choice of the length units, energies are given in effective Rydbergs. The Hamiltonian of the $N$ electrons in the stripe is then defined as follows:

$$H = -\frac{1}{r_s^2}\sum_{i=1}^{N}\nabla_i^2 + \sum_{i=1}^{N}\hat{\omega}_0^2 y_i^2 + \frac{2}{r_s}\sum_{i,j=1}^{N} V_{\mathrm{Coul}}(\mathbf{r_i}, \mathbf{r_j}). \tag{3.1}$$

The harmonic confinement parameter $\hat{\omega}_0 = \omega_0 r_s$ is scaled consistently with the coordinates. Note that for independent electrons this choice of the confinement would give a width of the wire $w(r_s) \propto 1/r_s$, therefore corresponding to maintaining constant the two dimensional density. The infinite extension along the $x$ direction is accounted for by using a modified version of the Ewald summation (see section 3.3). The assumption is that the diverging Coulomb repulsion is compensated by the interaction with a jellium of positive charge. We then consider a 2D array of such stripes in the limit of infinite separation.

## 3.2 Trial wavefunction

An important step in order to make a good DMC computation is find the a good trial wavefunction. A good choice of $\psi_T$ leads to smaller statistical error for the same amount of sampling. For a Fixed-node DMC computation the choice of $\psi_T$ becomes important in order to minimize the node-error.

In this work we used a trial wavefunction of the following form:

$$\psi_T(\mathbf{r}_1 \dots \mathbf{r}_N) = \prod_{i=1}^{N} u(y_i) \prod_{i<j}^{N} J(r_{ij}) \mathrm{Det}_{\uparrow} \phi_\alpha(\mathbf{r}_\beta) \mathrm{Det}_{\downarrow} \phi_\alpha(\mathbf{r}_\beta) \tag{3.2}$$

The Jastrow factor (JF) $J(r_{ij})$ is a simplified version of the form used in ref. [45]. The JF reduces the statistical error in both VMC and DMC for a given number of Monte Carlo steps. Otherwise the JF leaves the fixed-node DMC energy unchanged because the node of the trial wavefunction is not altered. In the original form the JF contains three terms: electron-electron $J_{ee}$, electron-nuclei $J_{en}$ and electron-electron-nuclei $J_{een}$. We only use the term $J_{ee}$:

$$J(r_{ij}) = exp(f_{ee}) = exp\left(\frac{b_1 R(r_{ij})}{1 + b_2 R(r_{ij})} + \sum_{p=2}^{N_{ord}} b_{p+1} R^p(r_{ij})\right) \tag{3.3}$$

The scaling function $R(r)$ is given by $r/(1+\kappa r)$. $N_{ord}$, the order of the polynomials, is taken to be 5. The number of parameters to be optimazed is reduced by the imposition of the electron-electron cusp condition: $b_1$ must be 1 for antiparallel-spin electrons and 1/3 for parallel spin electrons.

The one body factor $u(y) = exp(-c_1 y^2)$ is a Gaussian which is used to fine-tune an overall correction to the lateral width of the wavefunction.

The single particle functions are solutions of the non–interacting Hamiltonian:

$$\phi_\alpha(\mathbf{r}) = \psi^l_{ho}(y)\phi(x) \tag{3.4}$$

where $\psi^l_{ho}(y)$ are eigenstates of the harmonic oscillator of frequency $\hat{\omega}'_0$. The single particle functions $\phi(x)$ can be chosen to enforce the symmetry of the state considered. For simulating the liquid phase we use $\phi(x) = \exp(-ikx)$. The momentum $k$ is consistent with the periodicity of the system: $k = \pm n 2\pi/L$, with $n$ integer. Note that the energy levels of the non–interacting system show a band structure given by $\epsilon_{lk} = \hbar\hat{\omega}_0(l + 1/2) + \hbar^2 k^2/2m$, where $l$ plays the role of the band index. The number $N_b$ of harmonic oscillator bands filled depends on the density of the system, and must be determined from the Fermi energy of the $N$ particles. In the simulations we assumed that the filling of the bands is the same for the interacting and non-interacting electrons. We checked this assumption by computing the DMC energy for different fillings of the bands, always obtaining the lowest energy for the filling predicted for independent electrons.

In order to study the occurrence of a localized phase we implemented another set of single particle orbitals $\phi(x, x_j) = \exp[-c(x - x_j)^2]$, where $x_j$ are the localization centers located at $y = 0$ and distanced by $L/N$. Because we are considering an antisymmetrized product of such orbitals, this choice does not automatically correspond to constraining an electron around a given lattice site. If the orbitals are overlapping with each other an exchange of electrons is always possible.

In this thesis we used four wavefunctions (a), (b), (c) and (d). The differences among wavefunctions are summarized in table 3.1. The polarized wavefunction is defined as the product of two determinants, $\mathrm{Det}_{\uparrow}\phi_\alpha(\mathbf{r}_\beta)\mathrm{Det}_{\downarrow}\phi_\alpha(\mathbf{r}_\beta)$, one containing the coordinates of $N/2$ particles with spin up and the other containing the coordinates of $N/2$ particles with spin down. The polarized wavefunction includes a single determinant, in which there are the coordinates of all particles (with the same spin).

| | | |
|---|---|---|
| (a): | $\phi_\alpha(\mathbf{r}_\beta) = \psi^l_{ho}(y_\beta)\exp(-ik_\alpha x_\beta),$ | unpolarized liquid |
| (b): | $\phi_\alpha(\mathbf{r}_\beta) = \exp[-c(x_\beta - x_\alpha)^2]\exp[-c_2(y_\beta)^2],$ | unpolarized solid |
| (c): | $\phi_\alpha(\mathbf{r}_\beta) = \psi^l_{ho}(y_\beta)\exp(-ik_\alpha x_\beta),$ | polarized liquid |
| (d): | $\phi_\alpha(\mathbf{r}_\beta) = \exp[-c(x_\beta - x_\alpha)^2]\exp[-c_2(y_\beta)^2],$ | polarized solid |

Table 3.1: Differences among wavefunctions (a), (b), (c), (d). $c_2 = \hat{\omega}' + c$.

### 3.2.1 Optimization trial wavefunction

In this work we optimize the parameters $c$, $c_1$ and $\hat{\omega}'_0$, appearing in the wavefunction , by directly computing the energy for different values. Instead the Jastrow parameters are optimized using the *Newton* and *Linear* methods [46, 47] introduced by C. J. Umrigar and C. Filippi.

In the minimization process the set of wavefunction parameters $\mathbf{p}^0$ are changed of a quantity $\Delta\mathbf{p}$. Now we present two methods in order to optimize $\Delta\mathbf{p}$.

### Newton optimization method

The energy $E(\mathbf{p})$ is expanded to second order in the parameter $\mathbf{p}$ and $\mathbf{p}^0$,

$$E^{[2]}(\mathbf{p}) = E_0 + \sum_{i=1}^{N_{opt}} g_i \Delta p_i + \frac{1}{2} \sum_{i=1}^{N_{opt}} \sum_{j=1}^{N_{opt}} h_{ij} \Delta p_i \Delta p_j \tag{3.5}$$

where the sums are over all the parameters to be optimized, $\Delta p_i = p_i - p_i^0$ are the components of the vector of parameter variations $\Delta\mathbf{p}$, $g_i$ are the components of the energy gradient vector $\mathbf{g}$ and $h_{ij}$ are the elements of the energy Hessian matrix $\mathbf{h}$:

$$g_i = \left( \frac{\partial E(\mathbf{p})}{\partial p_i} \right) \qquad h_{ij} = \left( \frac{\partial^2 E(\mathbf{p})}{\partial p_i \partial p_j} \right) \tag{3.6}$$

Imposition of the stationary condition on expanded energy expression, $\frac{\partial^2 E(\mathbf{p})}{\partial p_i \partial p_j} = 0$, gives the following standard solution for the parameters variations:

$$\Delta\mathbf{p} = -\mathbf{h}^{-1} \cdot \mathbf{g} \tag{3.7}$$

where $\mathbf{h}^{-1}$ is the inverse of the Hessian matrix. In practice, eq. 3.7 gives the parameter variations $\Delta\mathbf{p}$ that are used to update the current wavefunction, $|\psi_0 > \rightarrow |\psi(\mathbf{p}^0 + \Delta\mathbf{p}) >$. This procedure has to be interacted until convergence is reached.

The Newton method is stabilized adding a positive constant $a_{diag}$ to the diagonal of the Hessian matrix $\mathbf{h}$

$$h_{ij} \rightarrow h_{ij} + a_{diag}\delta_{ij}$$

As $a_{diag}$ is increased the parameter variation $\Delta\mathbf{p}$ becomes smaller and rotates from the Newtonian direction to the steepest descent direction.

In eq. 3.7 we used as $g_i$ the components of the energy gradient vector and $h_{ij}$ the elements of the energy Hessian matrix. It is possible resolve the eq. 3.7 using gradient and Hessian of energy variance.

### Linear optimization method

The idea is to expand a normalized wavefunction $|\overline{\psi}(\mathbf{p})\rangle$ to first order in the parameters $\mathbf{p}$ around the current parameter $\mathbf{p}^0$:

$$|\overline{\psi}_{lin}(\mathbf{p})\rangle = |\psi_0\rangle + \sum_{i=1}^{N^{opt}} \Delta p_i |\overline{\psi}_i\rangle \tag{3.8}$$

where the wavefunction at $\mathbf{p} = \mathbf{p}^0$ is simply $|\overline{\psi}(\mathbf{p}^0)\rangle = |\overline{\psi}_0\rangle = |\psi_0\rangle$ (chosen to be normalized to 1) and, for $i \geq 1$, $|\overline{\psi}_i\rangle$ are the derivatives of $|\overline{\psi}(\mathbf{p})\rangle$ that are orthogonal to $|\psi_0\rangle$.

$$|\overline{\psi}_i\rangle = \left(\frac{\partial|\overline{\psi}(\mathbf{p})\rangle}{\partial p_i}\right)_{\mathbf{p}=\mathbf{p}^0} = |\overline{\psi}_i\rangle - S_{0i}|\overline{\psi}_0\rangle \tag{3.9}$$

where $S_{0i} = \langle\psi_0|\psi_i\rangle$. The minimization of the energy calculated with this linear wavefunction leads to the stationary condition of the associated Lagrange function:

$$\nabla_p[\langle\overline{\psi}_{lin}(\mathbf{p})|\hat{H}|\overline{\psi}_{lin}(\mathbf{p})\rangle - E_{lin}\langle\overline{\psi}_{lin}(\mathbf{p})|\overline{\psi}_{lin}(\mathbf{p})\rangle] = 0 \tag{3.10}$$

The Lagrange function is quadratic in $\mathbf{p}$ and equation 3.10 leads to the following generalized eigenvalue equation:

$$\overline{\mathbf{H}} \cdot \Delta\mathbf{p} = E_{lin}\overline{\mathbf{S}} \cdot \Delta\mathbf{p} \tag{3.11}$$

$\overline{\mathbf{H}}$ is th matrix of the Hamiltonian $\hat{H}$ in the $(N^{opt}+1)$-dimensional basis consisting of the current normalized wavefunction and its derivatives, $\overline{\mathbf{S}}$ is the overlap matrix of this $(N^{opt}+1)$-dimensional basis and $\Delta\mathbf{p}$ is the $(N^{opt}+1)$-dimensional vector of parameter variation with $\Delta p_0 = 1$. The linear method consists of solving equation 3.11 for the lowest eigenvalue and associated eigenvector $\Delta\mathbf{p}$.

The simple procedure of incrementing the set of parameters $\mathbf{p}$ by $\Delta\mathbf{p}$ is $\mathbf{p}_0 = \mathbf{p}_0 + \Delta\mathbf{p}$. It works for the linear parameters but it is not guaranteed to work for nonlinear parameters if the linear approximation of eq. 3.8 is not good. The Jastrow factor has nonlinear parameters. In this case is necessary to modify the standard procedure. A right choice of normalization of wavefunction can avoid the problem.

As the Newton optimization method it is possible to stabilize the minimization by adding a positive constant $a_{diag}$ to the diagonal of $\overline{\mathbf{H}}$ except for the first element.

## 3.3 Ewald Summation

Long range forces are a serious problem in numerical simulations, since no accurate results can obtained by using a finite box repeated periodically, unless an infinite sum over the particle images is performed. Long range forces are often defined as forces in which the spatial interaction falls of no faster than $r^{-d}$, where $d$ is the dimensionality of the system. In this category are for example the charge-charge interaction between electrons or ions, or the dipole-dipole interaction between molecules. A useful technique to avoid the problem when it is needed to sum the interaction between a charge and all its periodic images, is that of the so-called Ewald Summation [Ewald 1921; Madelung 1918]. In literature it is possible to find a lot about Ewald summation for systems periodic in 3D or 2D [48, 49, 50, 51], very little or nothing in the case of periodicity in one dimension. In this work we build a theoretical solution to the quasi-one dimensional case of the Ewald summation. Our task is to solve the problem for a 2D system of electrons with finite extent in one dimension and periodic in the other.

### 3.3.1 The procedure

Consider a 2D system periodic in one dimension and of finite extent in the other dimension, made of N electron and a uniform canceling background charge. The charge distribution, if there were one electron at $\mathbf{r_n}$ in the unit periodic cell is:

$$\rho(\mathbf{r}-\mathbf{r_n}) = \sum_{\mathbf{R}} \delta(\mathbf{r}-\mathbf{r_n}-\mathbf{R}) - \rho_{background}$$

where $\mathbf{R} = nL$ is the lattice translation vector with $n = 0, \pm 1, \pm 2...$, L is the periodicity of the system and $\rho_{background}$ is the background distribution charge (which makes each and every cell neutral).

What we want is to write the potential generated from this charge distribution in a useful way, due to the problems mentioned in the introduction. *The Ewald Method* consists in adding and subtracting to the charge distribution of the electron an array of Gaussian function, centered in $\mathbf{r_n}+\mathbf{R}$. This is just adding something which is zero. So we have:

$$\rho_{ewald}(\mathbf{r},\mathbf{r_n}) = \rho(\mathbf{r},\mathbf{r_n}) = \rho_1(\mathbf{r},\mathbf{r_n}) + \rho_2(\mathbf{r},\mathbf{r_n})$$

$$\rho_1(\mathbf{r},\mathbf{r_n}) = \left(\frac{1}{\mu\sqrt{\pi}}\right)^3 \sum_{\mathbf{R}} e^{-\frac{(\mathbf{r}-\mathbf{r_n}-\mathbf{R})^2}{\mu^2}} - \rho_{background}$$

$$\rho_2(\mathbf{r},\mathbf{r_n}) = \sum_{\mathbf{R}} \left(\delta(\mathbf{r}-\mathbf{r_n}-\mathbf{R}) - \left(\frac{1}{\mu\sqrt{\pi}}\right)^3 e^{-\frac{(\mathbf{r}-\mathbf{r_n}-\mathbf{R})^2}{\mu^2}}\right)$$

where $\mu$ is an arbitrary parameter that determines the width of the Gaussian distribution.

As it is possible to see in $\rho_2(\mathbf{r},\mathbf{r_n})$, the extra distribution acts like a screening positive charge. In this way, if $\mu$ is big enough, the interaction between neighboring electrons becomes a short range interaction due to the screening.

The potential due to $\rho_1(\mathbf{r},\mathbf{r_n})$ is calculated in reciprocal space and the one due to $\rho_2$ in the real space, both with the Poisson equation:

$$\nabla^2 \Phi_{ewald}(\mathbf{r},\mathbf{r_n}) = -4\pi \rho_{ewald}(\mathbf{r},\mathbf{r_n})$$

Solution of Poisson equation for $\rho_2(\mathbf{r},\mathbf{r_n})$ in real space gives:

$$\Phi_2(\mathbf{r},\mathbf{r_n}) = \sum_{\mathbf{R}} \frac{1 - erf\left(\frac{|\mathbf{r}-\mathbf{r_n}-\mathbf{R}|}{\mu}\right)}{|\mathbf{r}-\mathbf{r_n}-\mathbf{R}|}$$

Steps of the solution are shown in Section 3.3.2. Solution of Poisson equation for $\rho_1(\mathbf{r},\mathbf{r_n})$ in reciprocal space $\mathbf{k}=(k_x,k_y)$ (where $k_x=\frac{2\pi}{L}n, n=\pm1,\pm2,...$ is discrete due to the periodicity along x direction) gives:

$$\Phi_1(\mathbf{r},\mathbf{r_n})=\frac{4}{L}\sum_{k_x>0}cos(k_x(x-x_n))\int_0^{+\infty}dk_y\frac{1}{|\mathbf{k}|}erfc\left(\frac{\mu|\mathbf{k}|}{2}\right)cos(k_y(y-y_n))$$

Steps of the solution are shown in Section 3.3.3

Now we can write the Ewald potential in this way: $\Phi_{ewald}(\mathbf{r},\mathbf{r_n})=\Phi_1(\mathbf{r},\mathbf{r_n})+\Phi_2(\mathbf{r},\mathbf{r_n})+A(\mathbf{r_n})$ where the last term is added because the average potential in the cell must be zero, due to the neutrality of charge in the cell (see Section 3.3.4). Considering N electrons in the cell, the potential $\overline{\Phi}(\mathbf{r})$ generated in $\mathbf{r}$ by the N charges is found by superposing all the potentials for each charge component:

$$\overline{\Phi}(\mathbf{r})=\sum_{n=1}^{N}\Phi_{ewald}(\mathbf{r},\mathbf{r_n})$$

The potential acting on the charge $\mathbf{r_j}$ is:

$$\overline{\Phi}(\mathbf{r_j})=\sum_{n=1}^{N}\Phi_{ewald}(\mathbf{r_j},\mathbf{r_n})-\lim_{\mathbf{r}\to\mathbf{r_j}}\frac{1}{|\mathbf{r}-\mathbf{r_j}|}$$

where the second term is the divergent part of the self interaction of the electron in $\mathbf{r_j}$ with its own potential. It is possible to rewrite it in the following way:

$$\overline{\Phi}(\mathbf{r_j})=\sum_{n\neq j}^{N}\Phi_{ewald}(\mathbf{r_j},\mathbf{r_n})+\xi(\mathbf{r_j})$$

where $\xi(\mathbf{r_j})$ is the potential acting on the electron at $\mathbf{r_j}$ due to its own periodic images and canceling background (see Section 3.3.5).

$$\xi(\mathbf{r_j})=\lim_{\mathbf{r}\to\mathbf{r_j}}\left(\Phi_{ewald}(\mathbf{r},\mathbf{r_j})-\frac{1}{|\mathbf{r}-\mathbf{r_j}|}\right)\tag{3.12}$$

So the full Ewald potential energy appearing in Hamiltonians is the sum of the potential acting on all the N electron

$$U_{ewald}(\mathbf{r_1},...,\mathbf{r_N})=\frac{e^2}{2}\sum_{j=1}^{N}\overline{\Phi}(\mathbf{r_j})=\frac{e^2}{2}\sum_{j=1}^{N}\left(\sum_{n\neq j}^{N}\Phi_{ewald}(\mathbf{r_j},\mathbf{r_n})+\xi(\mathbf{r_j})\right)$$

If the screening that we force on the electrons is strong enough (i.e. $\mu$ is big enough) in the real space summation we do not have to consider the images of the electrons, it is just possible to consider only the term with $\mathbf{R}=0$.

### 3.3.2 Solution of Poisson equation for $\rho_2$

The equation to be solved is:

$$\nabla^2 \Phi_2(\mathbf{r}, \mathbf{r_n}) = -4\pi \sum_{\mathbf{R}} \left( \delta(\mathbf{r} - \mathbf{r_n} - \mathbf{R}) - \left( \frac{1}{\mu\sqrt{\pi}} \right)^3 e^{-\frac{(\mathbf{r}-\mathbf{r_n}-\mathbf{R})^2}{\mu^2}} \right)$$

with the condition that $\Phi_2$ goes to zero at infinity.
The equation splits into two equations. The first is the part with the $\delta$ function. The solution $\Phi_{2delta}$ is:

$$\Phi_{2delta}(\mathbf{r}, \mathbf{r_n}) = \sum_{\mathbf{R}} \frac{1}{|\mathbf{r} - \mathbf{r_n} - \mathbf{R}|}$$

The second part is with the Gaussian function with solution $\Phi_{2Gaus}$ . Due to symmetry reason, the solution $\Phi_{2Gauss}$ does not depend on the angles, so the Laplacian is:

$$\nabla^2 = \frac{1}{r^2} \frac{d}{dr} \left( r^2 \frac{d}{dr} \right)$$

If we look for a solution of the form:

$$\Phi_{2Gauss}(\mathbf{r}) = \frac{\chi(r)}{r}$$

the equation becomes:

$$\frac{d^2}{dr^2} \chi(r) = \frac{4}{\mu^3 \sqrt{\pi}} r \sum_{\mathbf{R}} e^{-\frac{(\mathbf{r}-\mathbf{r_n}-\mathbf{R})^2}{\mu^2}}$$

A solution of this equation with the correct boundary condition is:

$$\chi_{2Gauss}(r) = -\sum_{\mathbf{R}} erf \left( \frac{|\mathbf{r} - \mathbf{r_n} - \mathbf{R}|}{\mu} \right)$$

$$erf(x) = \frac{2}{\sqrt{\pi}} \int_0^x dt e^{-t^2}$$

therefore the solution for $\rho_2$ is:

$$\Phi_2(\mathbf{r}, \mathbf{r_n}) = \sum_{\mathbf{R}} \frac{1 - erf\left( \frac{|\mathbf{r}-\mathbf{r_n}-\mathbf{R}|}{\mu} \right)}{|\mathbf{r} - \mathbf{r_n} - \mathbf{R}|}$$

### 3.3.3 Solution of Poisson equation for $\rho_1$

It is possible to calculate this solution starting from the 2D result:

$$\frac{2\pi}{A}\sum_{\mathbf{k}}\frac{1}{|\mathbf{k}|}erfc\left(\frac{\mu|\mathbf{k}|}{2}\right)e^{-i\mathbf{k}\cdot(\mathbf{r}-\mathbf{r}_n)}$$

where $A$ is the area of the 2D plane.
We proceed therefore by considering a set of parallel quasi one-dimensional wires, distributed over the 2D layer. The distance between the wires is $c$.
In order to obtain the result of quasi one-dimensional case it needs to consider a unit cell of area $cL$ in which there is a single wire. Then you evaluate the limit $c \to \infty$ of the previous equation:

$$\begin{aligned}
\Phi_1(\mathbf{r},\mathbf{r_n}) &= \lim_{c\to\infty}\frac{2\pi}{cL}\sum_{k_x}\frac{1}{|\mathbf{k}|}erfc\left(\frac{\mu|\mathbf{k}|}{2}\right)e^{-i\mathbf{k}\cdot(\mathbf{r}-\mathbf{r}_n)} = \\
&= \frac{1}{L}\sum_{k_x}\int_{-\infty}^{+\infty}dk_y\frac{1}{|\mathbf{k}|}erfc\left(\frac{\mu|\mathbf{k}|}{2}\right)e^{-i\mathbf{k}\cdot(\mathbf{r}-\mathbf{r}_n)} = \\
&= \frac{4}{L}\sum_{k_x>0}cos(k_x(x-x_n))\int_{0}^{+\infty}dk_y\frac{1}{|\mathbf{k}|}erfc\left(\frac{\mu|\mathbf{k}|}{2}\right)cos(k_y(y-y_n))
\end{aligned}$$

### 3.3.4 Average potential in the cell equal to zero

We have to calculate the average potential in the cell and add a function $A$ to make it zero:

$$\langle\Phi_{ewald}(x,y)+A\rangle_{\varphi(x,y)}=0$$

where $\varphi(x,y)$ is the wavefunction of the positive background in the cell, i.e. the ground state of an harmonic oscillator along y direction (since the binding on the y direction is considered harmonic) times a plane wave along x direction (since along x direction the system is homogeneous):

$$\varphi(x,y)=\frac{1}{\sqrt{L}}\left(\frac{\alpha}{\pi}\right)^{\frac{1}{4}}e^{-\frac{\alpha}{2}y^2}e^{ik_xx} \qquad \alpha=\frac{m\omega}{\hbar}$$

So you obtain the follow expression for $A$:

$$A=A(\mathbf{r_n})=-\frac{1}{L}\left(\frac{\alpha}{\pi}\right)^{\frac{1}{2}}\int_{-\frac{L}{2}}^{+\frac{L}{2}}dx\int_{-\infty}^{+\infty}dy\sum_{\mathbf{R}}\frac{1-erf\left(\frac{|\mathbf{r}-\mathbf{r_n}-\mathbf{R}|}{\mu}\right)}{|\mathbf{r}-\mathbf{r_n}-\mathbf{R}|}e^{-\alpha y^2}$$

The function $A(\mathbf{r_n})$ must be calculated numerically.

### 3.3.5 Computation of $\xi$

$\xi(\mathbf{r_j})$ is the potential acting on the electron at $\mathbf{r_j}$ due to its own periodic images and canceling background:

$$\xi(\mathbf{r_j}) = \lim_{\mathbf{r}\to\mathbf{r_j}} \left( \Phi_{ewald}(\mathbf{r},\mathbf{r_j}) - \frac{1}{|\mathbf{r}-\mathbf{r_j}|} \right) =$$

$$= \sum_{\mathbf{R}\neq\mathbf{0}} \frac{1-erf\left(\frac{|\mathbf{R}|}{\mu}\right)}{|\mathbf{R}|} - \lim_{t\to 0}\frac{erf\left(\frac{t}{\mu}\right)}{t} + A(\mathbf{r_j}) +$$

$$+\frac{4}{L}\sum_{k_x>0}\int_0^{+\infty} dk_y \frac{1}{|\mathbf{k}|} erfc\left(\frac{\mu|\mathbf{k}|}{2}\right) =$$

$$= \sum_{\mathbf{R}\neq\mathbf{0}} \frac{1-erf\left(\frac{|\mathbf{R}|}{\mu}\right)}{|\mathbf{R}|} - \frac{2}{\mu\sqrt{\pi}} + A(\mathbf{r_j}) + \frac{4}{L}\sum_{k_x>0}\int_0^{+\infty} dk_y \frac{1}{|\mathbf{k}|} erfc\left(\frac{\mu|\mathbf{k}|}{2}\right)$$

### 3.3.6 Implementation of Ewald Summation

The implementation of Ewald Summation was very difficult. First of all it is necessary to tabulate all the contributions in order to minimize the computing time machine, in particular the integral terms.

The calculation of $A(\mathbf{r_n})$ is very heavy, because wide oscillation in the integrand make difficult to reach a convergence. After many attempts the problem was resolved using the Gauss-Laguerre Quadrature method. The idea of Gaussian Quadratures [52] is rewrite the a defined integral in the following way:

$$\int_a^b W(x)f(x)dx \approx \sum_{j=0}^{N-1} w_j f(x_j) \tag{3.13}$$

We can arrange the choice of weights $w_j$ and abscissas $x_j$ to make the integral exact for a class of integrands. In numerical analysis Gauss-Laguerre quadrature is an extension of Gaussian quadrature method for approximating the value of integrals of the following kind:

$$\int_0^\infty e^{-x} f(x)dx \tag{3.14}$$

In this case

$$\int_0^\infty e^{-x} f(x)dx \approx \sum_{i_1}^{n} w_i f(x_i) \tag{3.15}$$

where $x_i$ is the i-th root of Laguerre polynomial $L_n(x)$.

The second important step is to choose the optimal value for $\mu$. That is a parameter modulating the screening effect of Gaussians. We chose the value of $\mu$ that minimizes the dependence of energy on the number of electron $N$.

We found that a good value of $\mu$ is $L/5$, where $L$ is the side of the simulation cell. This value does not differ from the heuristically determined value that is commonly presented for 2D and 3D simulations.

We chose to perform the simulations using different numbers of electrons in order to have a direct controll on how much the potential contribution depend on $N$. In the table 4.1 there is the value of energy at $r_s$=5 for different numbers of electron, $N$=50, 75, 98. This example shows the energy depends on $N$ and it involves a change in energy of order $10^{-4}$. The important aspect is the difference in energy if you make a computation with $N$ =73 or 75 is smaller then error.

## 3.4 CHAMP

The program used to study the ground-state properties of the two-dimensional electron gas laterally confined was based on CHAMP[1]. CHAMP is a Quantum Monte Carlo suite of programs for electronic structure calculations on a variety of systems (atoms, molecules, clusters, solids and nanostructures) written by Cyrus Umrigar, Claudia Filippi and, with smaller contributions, by a few others. CHAMP is presently a suite of 11 programs that have the following 3 basic capabilities:

1. Optimization of many-body wave functions by variance minimization (FIT)
2. Metropolis or Variational Monte Carlo (VMC)
3. Diffusion Monte Carlo (DMC).

In order to use Champ for compute the laterally confined 2D electron gas it was necessary to make substantial changes in the code. The bigger change was the introduction of Ewald summation (see section 3.3) for the potential computation. Then we fixed the periodicity only in one dimension using the *periodic boundary condition*. We wrote the wavefunction (see section 3.2), except the Jastrow factor.

### 3.4.1 Particularly noteworthy features of CHAMP

Efficient wavefunction optimization by the variance-minimization method. For finite systems the capability exists to optimize not only the Jastrow part of the wavefunction but the determinantal part (CI coefficients, orbital coefficients and orbital exponents) as well.

---

[1] http://www.ccmr.cornell.edu/ cyrus/champ.html

a) Optimized Trial Wave Functions for QMC calculation [53].

b) A Method for Determining Many-Body Wavefunctions[54],

A variety of forms of the Jastrow factor that introduce e-n, e-e and e-e-n correlations (e=electron, n=nucleus), including forms that are systematically improvable (within the constraint due to using no more than e-e-n correlations) and that obey all three types of cusp conditions exactly. For large systems the option exists to use Jastrow functions that go exactly to a constant beyond some distance, thereby improving the scaling of the computer time with system size[53, 54, 55]

An accelerated Metropolis method that allows one to make very large moves and still have a high acceptance, resulting in very short autocorrelation times. The gain, compared to other Metropolis methods is particularly large when pseudo potentials are not used[56, 57].

A very efficient diffusion Monte Carlo algorithm that takes into account the singularities in the local energy and velocity at nodes of the wavefunction and at particle coincidences. The gain, compared to other Metropolis methods is particularly large when pseudo potentials are not used[58].

# Chapter 4

# Ground state properties of the laterally confined 2D electron gas

Simulations have been performed using different numbers of electrons, at different values of the density, parametrized by the Wigner-Seitz radius $r_s$, and at different value of confinement parameter $\omega_0$. The confinement parameter has been chosen to be $\hbar\omega_0 = 2, 4, 6$ meV $(= 0.338, 0.674, 1\ \text{Ry}^*)$.

As previously exposed in the chapter 3, in a QMC simulation it is necessary to choose a good trial wavefunction, to be used as importance function and starting point for the projection. For the confined 2D electron gas, we use the combination of plane wave, Gaussian orbitals and Jastrow correlations described in chapter 3. The structure of the wavefunction is the same both for the antiferromagnetic and for ferromagnetic state considered. For the case in which electrons are localized (Wigner crystal states) the plane waves are replaced by Gaussians in the longitudinal direction.

When the lateral confinement is strong it is possible to identify a single relevant parameter determining the properties of the wire, i.e. is the ratio between the gap in the single particle levels in the harmonic confining potential, and the Fermi energy of the electrons in the longitudinal direction $C_F = 2m\hbar\omega_0/\hbar^2 k_F^2$[59], which in effective atomic units reduces to $32 r_s^2 \omega_0/\pi^2$. Therefore, at least in the strongly one-dimensional regime $C_F >> 1$, the results should approximately be independent of the specific value of $\omega_0$ and scale as a function of $C_F$. However, this is not true at high densities, where more than one harmonic oscillator band is occupied.

We thoroughly studied the dependence of the results of the finite size, that might come from the use of Ewald sums for the potential energy. At the end of this analysis we concluded that for $N \geq 74$ such effects are already well reduced. $N = 74$ and $N = 98$ are the sizes employed in must of the simulation performed.

We also chose $\tau = 0.001$, where $\tau$ is the diffusion step, in order to minimize the time step error.

### 4.0.2 Results at $\hbar\omega_0 = 4$meV

In Tab. 4.1 we report the energy per electron computed with $N = 74$ and 98 electrons at different values of $r_s$.

For the unpolarized liquid phase the number of harmonic oscillator bands used in the wavefunctions is 3 for $r_s = 0.5$, and 1 for $r_s > 1$, while for the polarized liquid phase we fill 5 bands for $r_s = 0.5$, 2 for $r_s = 1$, and one for $r_s > 1$. In the localized phase we consider localized orbitals, and we assume that the correct density is reached by varying the parameters of the Gaussians.

As it can be seen, at high densities ($r_s < 3$) the ground state is an unpolarized liquid. In particular for $r_s \leq 1$ the $C_F$ parameter is rather small, and the system has a two–dimensional character.

For $r_s \geq 5$ the ground state is found to be the spin–polarized, with an energy gap of the order 1mRy$^*$. However, for a given polarization, the liquid and crystal phases have extremely close energies. This very small difference (<0.1mRy$^*$) might be taken as a conservative estimate of the fixed node error, suggesting that the energy gap between the polarized and unpolarized phases is robust. However, it is not possible within our current numerical accuracy to draw a definite conclusion about the occurrence of Wigner crystallization.

In Fig. 4.1 we report the computed energies, together with the fit of the total energy according to the Tanatar-Ceperley[60] functional in the range of 2D densities corresponding to an estimate of the electron density of the wire. As it can be seen, at low values of $r_s$, the energy of the electrons in the wire becomes closer and closer to that of the equivalent homogeneous 2D system. The discrepancies are due to the approximate way in which the width of the wire is determined. On the other hand, the figure clearly displays that in the high $r_s$ regime the energies of the four phases considered strongly deviates from the 2D value, and tend to collapse on a single value, consistently with the fact that we are approaching an effective 1D regime ($C_F \to \infty$).

A problem occurring in QMC simulations of quasi 1D systems is the lack of ergodicity due to the extremely low exchange rate between electrons[31]. We tried to assess the existence of this drawback in our 2D simulations. This was achieved both by direct inspection, i.e. by checking the diffusion of close pairs of electrons, and looking at the Monte Carlo mean square diffusion of the electrons along the wire, estimated by:

$$\langle(\mathbf{x} - \mathbf{x_0})^2\rangle = \frac{1}{NM}\sum_{j=1}^{M}\sum_{i=1}^{N}[\mathbf{x}_{j,i}(\tau) - \mathbf{x}_{0,i}]^2 \tag{4.1}$$

where $\mathbf{x}_{0,i}$ and $\mathbf{x}_{j,i}(\tau)$ (with $\tau = M\Delta\tau$, $\Delta\tau$ is the time step used in the DMC simulation, $\Delta\tau = 0.001$ and $M = 175000$) are the $x$ coordinate of the initial and final positions of the electron $i$ after $j$ DMC steps.

| N,$r_s$ | 0.5 | 1 | 2 | 3 | 5 | 7 |
|---|---|---|---|---|---|---|
| 50 (a) | | | | | -0.095596(6) | |
| 74 (a) | -0.5288(4) | -0.36810(5) | -0.26760(3) | -0.19458(3) | -0.09549(1) | -0.026681(7) |
| 98 (a) | -0.5513(4) | -0.36800(8) | -0.26750(3) | -0.19453(2) | -0.09544(1) | -0.026791(7) |
| 50 (b) | | | | | -0.09647(1) | |
| 74 (b) | -0.4163(6) | | -0.26527(3) | -0.19465(1) | -0.096476(8) | -0.027629(5) |
| 98 (b) | -0.3979(8) | | -0.26518(3) | -0.19460(1) | -0.096491(7) | -0.027634(5) |
| 49 (c) | | | | | -0.09787(1) | |
| 73 (c) | -0.0424(4) | -0.20522(5)* | -0.21482(1) | -0.19067(1) | -0.097797(6) | -0.028524(4) |
| 97 (c) | -0.0443(4) | -0.20697(8) | -0.21524(1) | -0.19077(1) | -0.097695(6) | -0.028500(4) |
| 49 (d) | | | | | -0.09772(1) | |
| 73 (d) | | | | -0.18999(1) | -0.097671(6) | -0.028423(6) |
| 97 (d) | | | | -0.19000(1) | -0.097673(5) | -0.028405(4) |

Table 4.1: Total energy per electron (in effective Rydberg) for a laterally confined two dimensional electron gas with $\hbar\omega_0$=4meV. (a): unpolarized liquid wavefunction. (b): localized wavefunction. (c): polarized liquid wavefunction. (d): polarized solid wavefunction. (*): N=74.

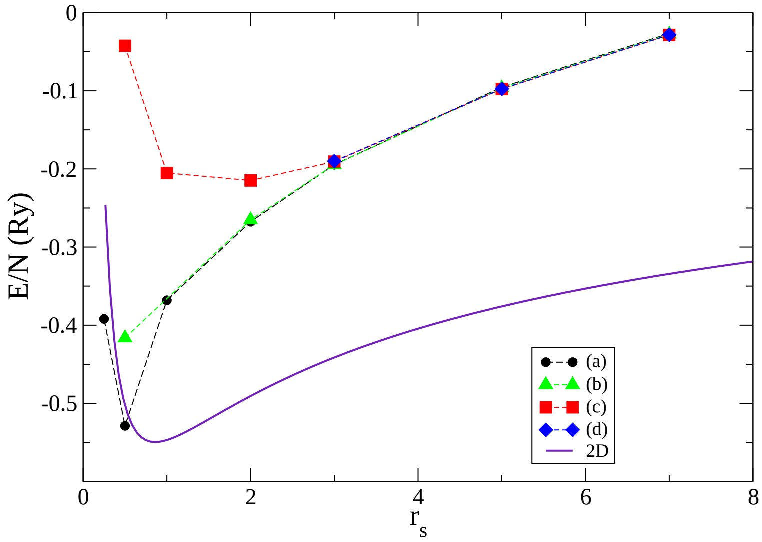

Figure 4.1: Total energy per electron (in effective Rydberg) for a laterally confined two dimensional electron gas. Dots: unpolarized fluid; triangles: unpolarized crystal; squares: polarized fluid; diamonds: polarized crystal. The full line is the energy of the 2D system at a value of $r_s^{2D}$ estimated from the width of the lateral density of electrons. We report also an estimation of energy at $r_s = 0.25$.

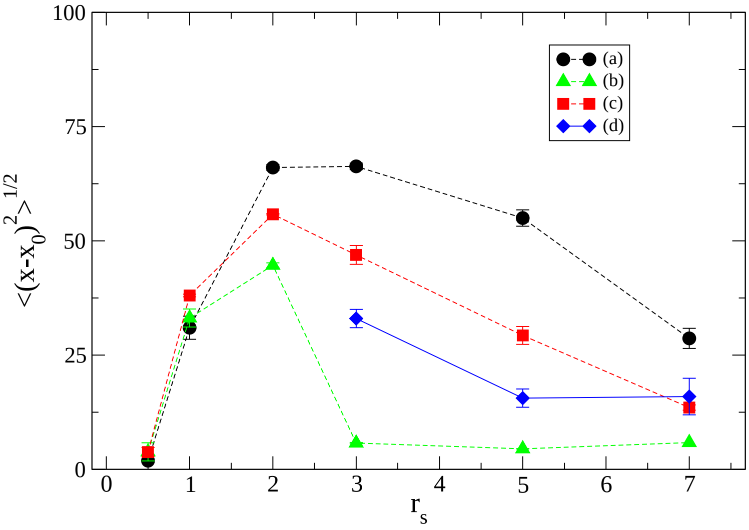

Figure 4.2: QMC diffusion of the electrons in the wire (in units of $a_0^*$) as a function of $r_s$ at $\hbar\omega_0 = 4$meV. The points display the computed diffusion for the unpolarized liquid (dots), polarized liquid (squares), localized (triangles) and polarized solid (diamonds) phases.

In Fig. 4.2 we report the evaluation of this quantity as a function of $r_s$ for the four phases considered. In this picture the $x$ coordinates are in units of $a_0^*$ in order to avoid the rescaling effect of box size. For $r_s \leq 2$ the diffusion of electrons is very active. The dependence on $r_s$ (almost linear for the unpolarized liquid phase) is given by the increased size of the wire in the longitudinal direction. This is a clear sign of the fact that electrons are allowed to almost freely diffuse for the whole length of the wire. For $r_s \geq 3$ the diffusion ceases to increase. When using localized orbitals, it is clear how the diffusion converges to a constant value much lower than the values seen in the liquid phase, indicating that electrons remain strongly localized around lattice sites.

In figure 4.3 there are two examples of the random walks described by two neighboring electrons during the simulation. Both figures represent the liquid phase at low density ($r_s = 5$) for pairs of electrons with opposite spin (fig. 4.3, top) and same spin (fig. 4.3, bottom). The reciprocal crossing is evident in both cases.

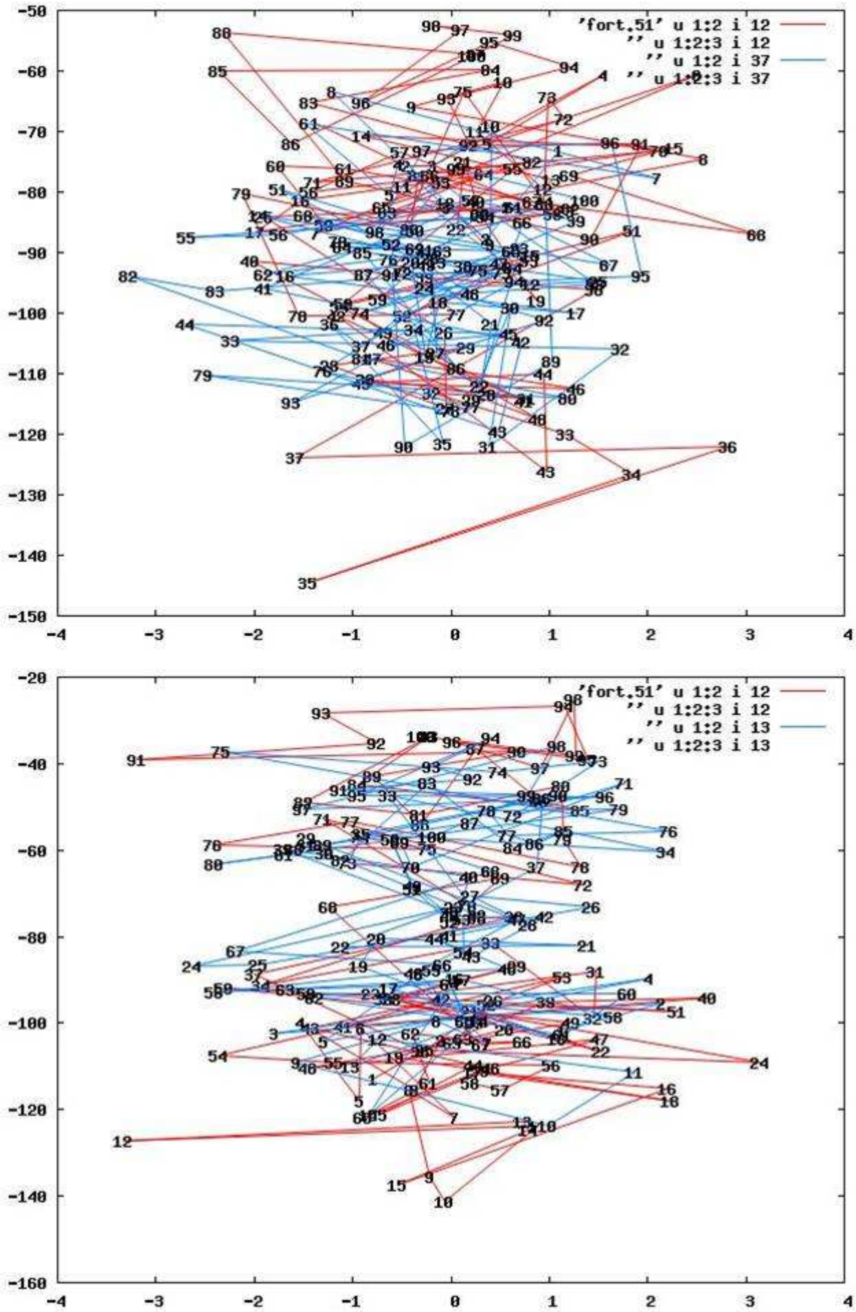

Figure 4.3: Electron displacements in liquid phase at low density ($r_s = 5$) for pair of electrons with opposite spin (top) and with same spin (bottom)

In Fig. 4.4 we report the transverse electron density for two different values of $r_s$ and the transverse jellium density. The picture shows how the system becomes effectively narrower with increasing $r_s$. For $r_s = 0.5$ the system is almost two dimensional, in agreement with the fact that the energy of the confined system approaches the energy of the 2D system. For lower densities, the effect of the confinement on the energy becomes stronger and stronger.

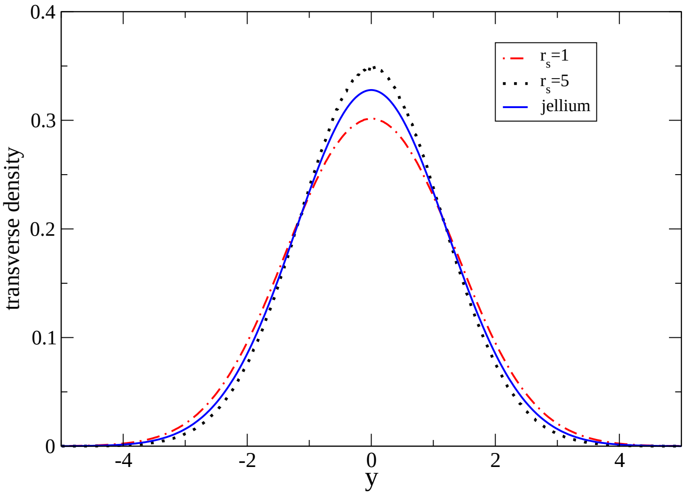

Figure 4.4: Transverse density in the confined 2D electrons gas. The density computed by DMC is compared with the "jellium" density, i.e. from the density given by the ground state solution of the confining harmonic potential. Curves are given for $r_s = 1$ (dotted and dashed-dotted line), and $r_s = 5$ (full and dashed lines). $y$ is given in units of $a_0^*$

In figure 4.5 the pair correlation function, $g(x)$, for $r_s = 1$ and $r_s = 5$ is displayed. $g(x)$ is computed along the longitudinal coordinate $x$ and integrated in the transverse coordinate $y$. Decreasing the density, $g(x)$ shows wide oscillations.

In figure 4.6 we show the electron spin density $r(x)$, computed in the longitudinal direction, for two different densities ($r_s = 1$ and $r_s = 5$), and computed using localized wavefunction. $r(x)$ is the probability that an electron with a fixed spin is at position $x$. We find that by increasing the electron density, the number of exchanges increases. At high density ($r_s = 1$) the electron density displays a modulation, but electrons are spread all over the wire. At low density ($r_s = 5$) electrons are clearly localized around lattice sites.

In order to better understand the scaling of the system with density and confinement about this system we decided to study it with $\hbar\omega_0$=2 meV and 6 meV.

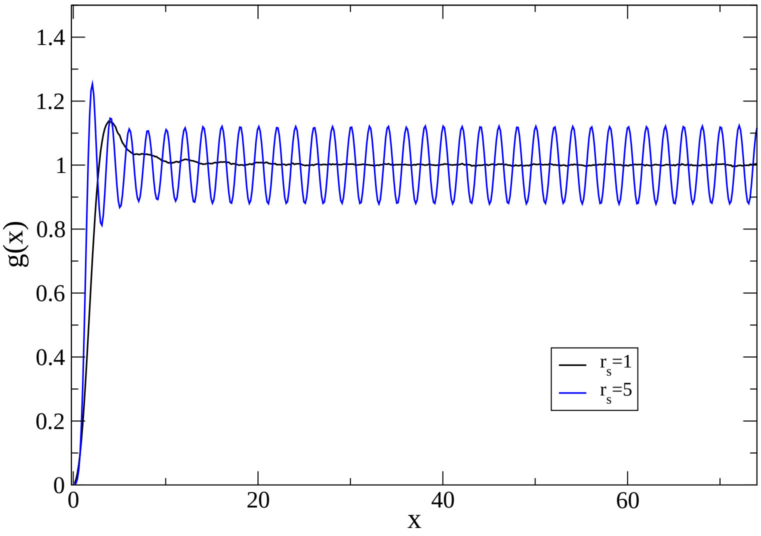

Figure 4.5: Pair correlation function for $r_s = 1$ and $r_s = 5$.

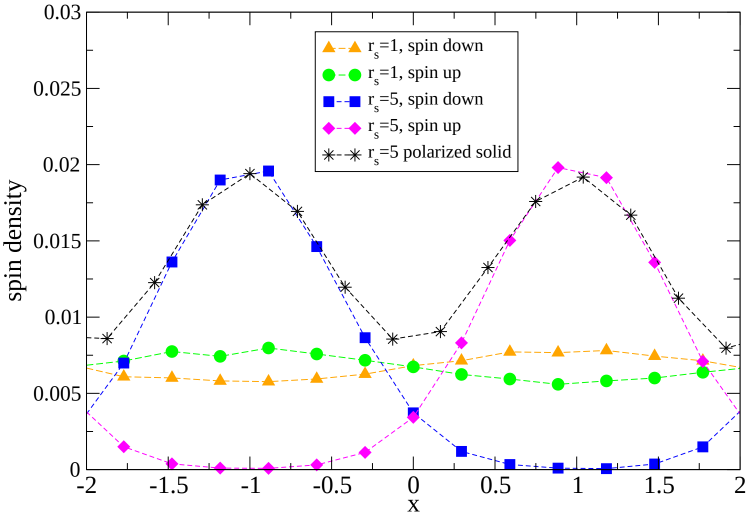

Figure 4.6: Spin density function for $r_s = 1$ and $r_s = 5$.

### 4.0.3 Results at $\hbar\omega_0 = 2$meV and $\hbar\omega_0 = 6$meV

We studied the equation of state for two other values of confining parameter $\omega_0$. In order to understand how our model behaves changing the lateral confinement. We proceeded to study the system for $\hbar\omega_0 = 2, 6$ meV in the same way we did for $\hbar\omega_0 = 4$ meV.

The same algorithm to fill up the orbitals of wavefunction was employed. At $\hbar\omega_0 = 2$meV for the unpolarized liquid phase the number of harmonic oscillator bands used in the wavefunctions is 4 for $r_s = 0.5$, 2 for $r_s = 1$, and one for $r_s \geq 2$, while for the polarized liquid phase we fill 7 bands for $r_s = 0.5$, 3 for $r_s = 1$, and one for $r_s > 1$. At $\hbar\omega_0 = 6$meV, for the unpolarized liquid phase the number of harmonic oscillator bands used in the wavefunctions is 3 for $r_s = 0.5$, and one for $r_s \geq 1$, while for the polarized liquid phase we fill 5 bands for $r_s = 0.5$, 2 for $r_s = 1$, and one for $r_s > 1$.

We report in table 4.2 the equation of state for $\hbar\omega_0$=2meV and in table 4.3 the equation of state for $\hbar\omega_0$=6meV. Comparing tables 4.2, 4.1 ,4.3 it is possible to observe that increasing $\omega_0$ the density at which the liquid phase ceases to exist shifts to higher density and at $r_s \geq 3$ the system is always polarized.

A deeper analysis shows that at $\hbar\omega_0 = 6$meV for $r_s < 3$ the system is still liquid. It is possible to understand this observation by looking at the figures 4.7, 4.8 and 4.9.

Fig. 4.7 shows the QMC diffusion of the electrons in the wire as a function of $r_s$ at $\hbar\omega_0 = 6$meV. The black dots and the green triangles are very close for $r_s < 3$, meaning that the system behaves in a similar way either using the unpolarized liquid wavefunction or solid wavefunction. The wavefunction for a solid is built starting from orbitals localized on given lattice sites. However, the Pauli principle (implemented in the construction of a Slater determinant) yields the electron exchange, that is frequent at high densities.

| N,$r_s$ | 0.5 | 1 | 2 | 3 | 5 | 7 |
|---|---|---|---|---|---|---|
| 72 (a) | -0.7687(4) | -0.4636(1) | | | | |
| 73 (a) | | | -0.33693(2) | -0.27728(1) | -0.20086(1) | -0.148749(6) |
| 96 (a) | -0.7449(4) | -0.4605(3) | | | | |
| 98 (a) | | | -0.33705(2) | -0.27726(2) | -0.20080(1) | -0.14871(1) |
| 74 (b) | -0.4679(7)* | | -0.33125(2) | -0.27458(1) | -0.203092(7) | -0.149657(4) |
| 98 (b) | | | -0.33136(2) | -0.27460(2) | -0.203087(7) | -0.149658(5) |
| 73 (c) | -0.4181(4) | -0.3737(2) | -0.25989(1) | -0.26576(1) | -0.203839(7) | -0.150329(4) |
| 97 (c) | | -0.3720(3) | -0.25876(1) | -0.26574(1) | -0.203812(7) | -0.150316(4) |
| 73 (d) | | | | -0.26494(1) | -0.202332(7) | -0.147502(7) |
| 97 (d) | | | | -0.26496(1) | -0.202330(7) | -0.147564(7) |

Table 4.2: Total energy per electron (in effective Rydberg) for a laterally confined two dimensional electron gas with $\hbar\omega_0$=2meV. (a): unpolarized liquid wavefunction. (b): localized wavefunction. (c): polarized liquid wavefunction. (d): polarized solid wavefunction. (*): $N = 72$.

| N,$r_s$ | 0.5 | 1 | 2 | 3 | 5 | 7 |
|---|---|---|---|---|---|---|
| 74 (a) | -0.3040(4) | -0.28103(5) | -0.16975(4) | -0.08584(3) | 0.03041(1) | 0.108615(6) |
| 98 (a) | -0.3042(4) | -0.28217(5) | -0.16974(4) | -0.08564(3) | 0.03052(1) | 0.108659(6) |
| 74 (b) | -0.3951(6) | -0.2960(3) | -0.16970(4) | -0.08619(2) | 0.029973(8) | 0.108301(5) |
| 98 (b) | -0.3816(6) | -0.2922(2) | | -0.08627(2) | 0.029964(9) | 0.108300(4) |
| 73 (c) | 0.3158(4) | | -0.12901(2) | -0.08457(1) | 0.028429(7) | 0.107428(5) |
| 74 (c) | | -0.02518(5) | | | | |
| 97 (c) | 0.3346(5) | | -0.12951(2) | -0.08452(1) | 0.028459(7) | 0.107441(4) |
| 98 (c) | | -0.02575(6) | | | | |
| 73 (d) | | | | -0.08385(1) | 0.028588(4) | 0.107971(4) |
| 97 (d) | | | | -0.08382(1) | 0.028608(7) | 0.107958(4) |

Table 4.3: Total energy per electron (in effective Rydberg) for a laterally confined two dimensional electron gas with $\hbar\omega_0$=6meV. (a): unpolarized liquid wavefunction. (b): localized wavefunction. (c): polarized liquid wavefunction. (d): polarized solid wavefunction.

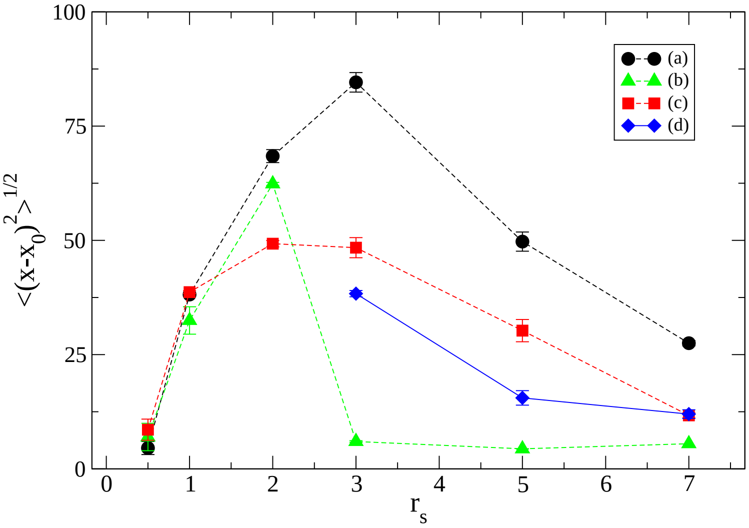

Figure 4.7: QMC diffusion of the electrons in the wire (in units of $a_0^*$) as a function of $r_s$ at $\hbar\omega_0$ = 6meV. The points display the computed diffusion for the unpolarized liquid (dots), polarized liquid (squares), localized (triangles) and polarized solid (diamonds) phases.

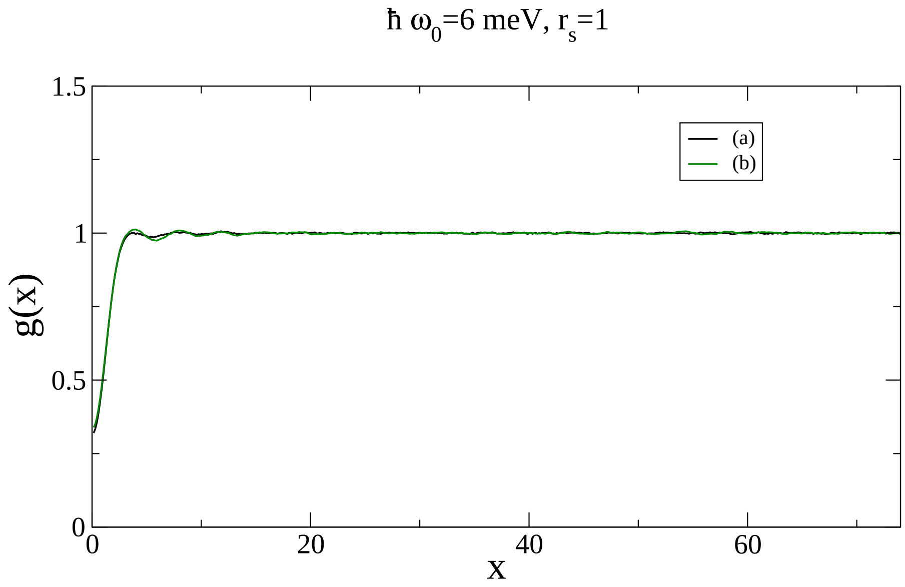

Figure 4.8: Pair correlation function for $r_s = 1$ at $\hbar\omega_0 = 6$meV. The points display the $g(x)$ computed with the unpolarized liquid (a) and solid (b) wavefunction.

In Fig. 4.8 and 4.9 the pair correlation function $g(x)$ for $r_s = 1$ and $r_s = 3$ at $\hbar\omega_0 = 6$meV are shown. In both figures there are the $g(x)$ computed using unpolarized liquid and localized wavefunction. At $r_s = 1$ a different choice of wavefunction along $x$ (plane wave or Gaussians) leads to a pair distribution function $g(x)$ that it always displays the typical features of a liquid. For $r_s = 3$ (Fig. 4.9) the difference between the pair functions computed starting from different wavefunctions is evident and then the solid structure of $g(x)$ computed with unpolarized solid wavefunction becomes clear.

In figure 4.10 we also report the QMC diffusion of the electrons at $\hbar\omega_0 = 2$meV. This picture confirms the liquid–like behavior of the system for $r_s \leq 3$. For the unpolarized liquid phase the diffusion linearly increases with $r_s$ indicating that on average the exchange of electrons is very active. For $r_s > 3$ the diffusion ceases to increase. In the solid phase it is clear how for $r_s > 2$ the diffusion ceases to increase and converges to constant values much lower (about one order of magnitude) than the values seen in the liquid phase, indicating that electrons are strongly localized around lattice sites. The polarized liquid phase shows a strange behavior as a function of $r_s$. There is a strong connection between the wavefunction parameters and the QMC diffusion. For example the low value of QMC diffusion at $r_s = 2$ for polarized liquid phase is due to the choice of parameter $c_1$ ($u(y) = exp(-c_1 y^2)$, see Eq. 3.2). The parameter $c_1$ can be used to give an overall correction to the lateral width of the wave function. Generally this parameter is useful at high density. It is necessary to choose a

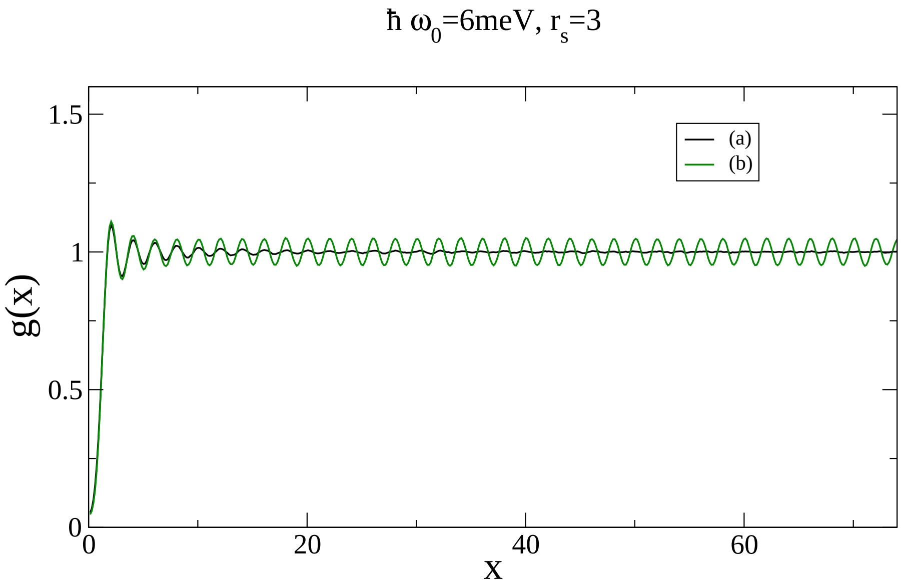

Figure 4.9: Pair correlation function for $r_s = 3$ at $\hbar\omega_0 = 6$meV. The points display the $g(x)$ computed with the unpolarized liquid (a) and solid (b) wavefunction.

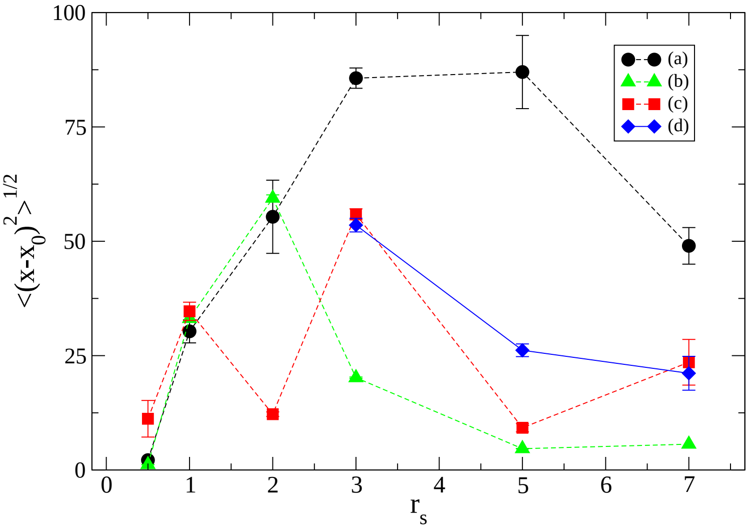

Figure 4.10: QMC diffusion of the electrons in the wire (in units of $a_0^*$) as a function of $r_s$ at $\hbar\omega_0 = 2$meV. The points display the computed diffusion for the unpolarized liquid (dots), polarized liquid (squares), localized (triangles) and polarized solid (diamonds) phases.

low value of $c_1$. However, a small variation in $c_1$ implies an high variation in the walker's capacity to diffuse. So this parameter is useful, but very difficult to use.

At $\hbar\omega_0 = 2$ meV, as at $\hbar\omega_0 = 4$ meV, we do not report the unpolarized solid value at $r_s = 1$, due to unresolved computational difficulties. At $r_s = 1$ the system is a unpolarized liquid. Using a solid wavefunction we are not able to obtain a stable value for the energy.

Another previous feature is the energy value at $\hbar\omega_0 = 2$ meV and $r_s = 0.5$, $E/N = -0.7687(4)$ Ry*. This value looks unexpected because it is lowest of every energy value of equation of state of the two–dimensional homogeneous electron gas. By confining the two-dimensional electron gas one might expect to obtain an energy higher than the 2D equation of state. This result can be justified by the use of Ewald Summation. In Ewald Summation the positive charge background is chosen arbitrarily, with the only condition of charge neutrality. This fact can introduce an overall shift of the energies with respect to the case of the homogeneous system.

The following figures (4.11 - 4.14) show selected pair correlation functions as function of $r_s$ and $\omega_0$, computed using different trial wavefunctions. In Fig. 4.11 pair correlation function for $r_s = 3, 5, 7$ at $\hbar\omega_0 = 6$meV for the polarized liquid phase is shown. In the Fig. 4.12 we display the pair correlation function for $r_s = 3, 5, 7$ at $\hbar\omega_0 = 6$meV for the localized phase. Comparing the two pictures it comes clear how the two type of wave functions work in our model.

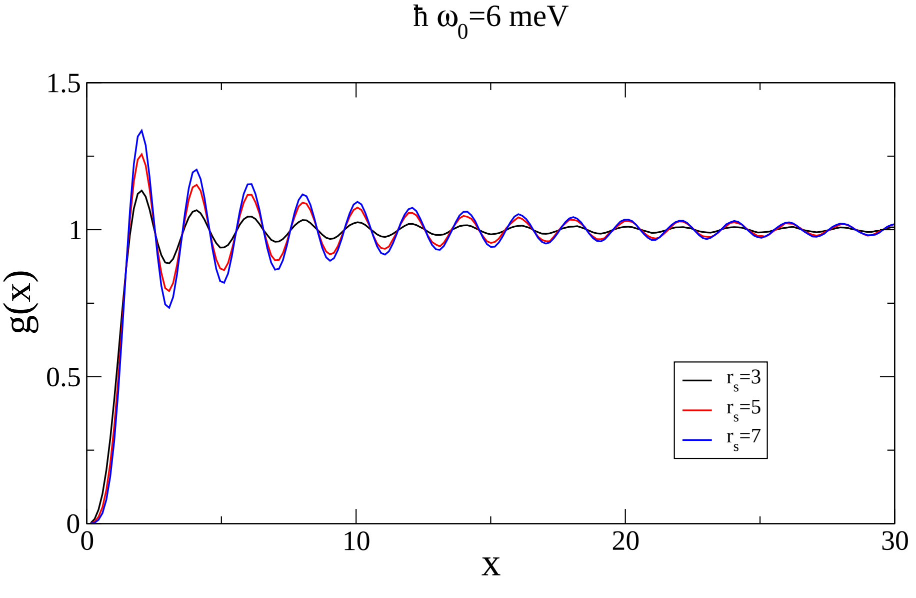

Figure 4.11: Pair correlation function for $r_s = 3, 5, 7$ at $\hbar\omega_0 = 6$meV. The points display the $g(x)$ computed with the polarized liquid wavefunction.

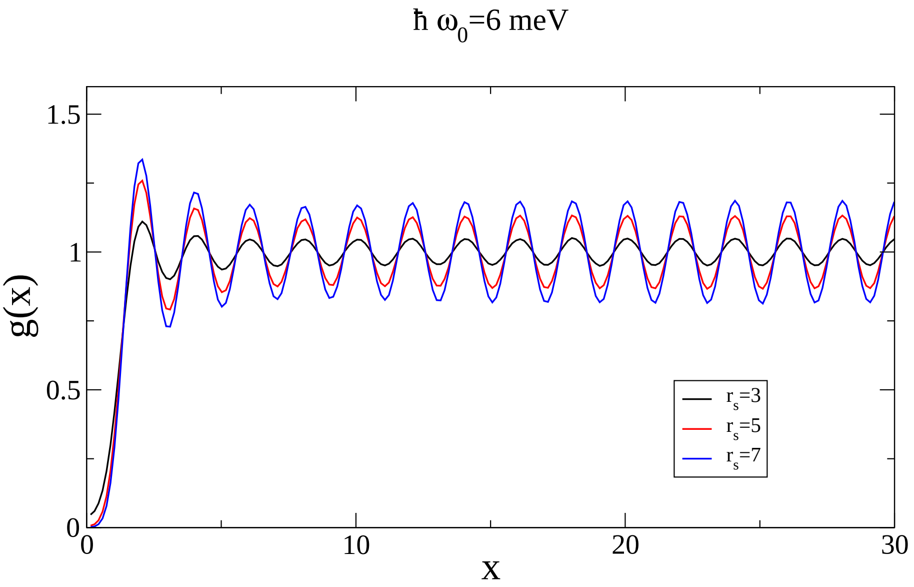

Figure 4.12: Pair correlation function for $r_s = 3, 5, 7$ at $\hbar\omega_0 = 6$meV. The points display the $g(x)$ computed with the unpolarized solid wavefunction.

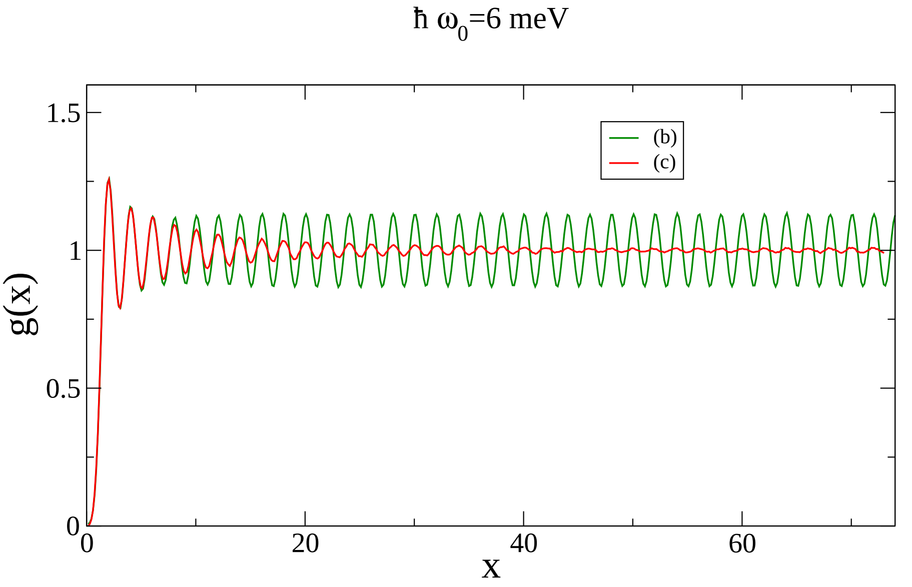

Figure 4.13: Pair correlation function for $r_s = 5$ at $\hbar\omega_0 = 6$meV. The points display the $g(x)$ computed with the polarized liquid (c) and unpolarized solid (b) wavefunction.

The unpolarized solid wavefunction shows a $g(x)$ typical of a strong localized electron system. Increasing $r_s$ the system becomes more localized, as expected in a Wigner crystal. The polarized liquid wavefunction shows a $g(x)$ with oscillations, which are wide for small value of $x$. The shape of these $g(x)$ indicates that the system tends to reproduce a solid structure.

A direct comparison between the solid and the polarized phase is show in Fig. 4.13 and 4.14. Both figures represent the pair correlation function $g(x)$, computed for the polarized liquid and for the localized phase, at $r_s = 5$. The difference between the two figures is the value of $\omega_0$. The two figures are very similar. It is possible to observe that the peaks in $g(x)$ are at the same values of $x$ for the polarized and solid wavefunction. Increasing $x$ the only observable difference is the damping of the oscillations of $g(x)$ computed with polarized wavefunction.

Fig. 4.15 represents the transverse density for $r_s = 5$ and $\hbar\omega_0 = 2, 4, 6$ meV. This picture shows in a clear way the effect of changing the confinement parameter $\omega_0$ in our model. Increasing $\omega_0$ we force the electrons to stay more close to the longitudinal axis of the wire.

## 4.1 Overview

Comparing the results at $\hbar\omega_0$ =2, 4, 6 meV, we can say the system is a polarized and localized at $r_s > 3$ and unpolarized liquid at $r_s < 3$. Increasing $\omega_0$ the system tends to become more localized, but at high density the electron exchange persists.

Our results strongly support the onset of a polarized phase. More checks at high values of $\hbar\omega_0$ (as 40-80 meV) are performed. Preliminary results show that polarization does not vanish. However the current version of the code does not permit us to do rigorous calculation at high values of $\omega_0$.

At high density the system is not crystallized due to electron exchange. However, the density modulations displayed in Fig. 4.6 may suggest the occurrence of a spin–wave ground state.

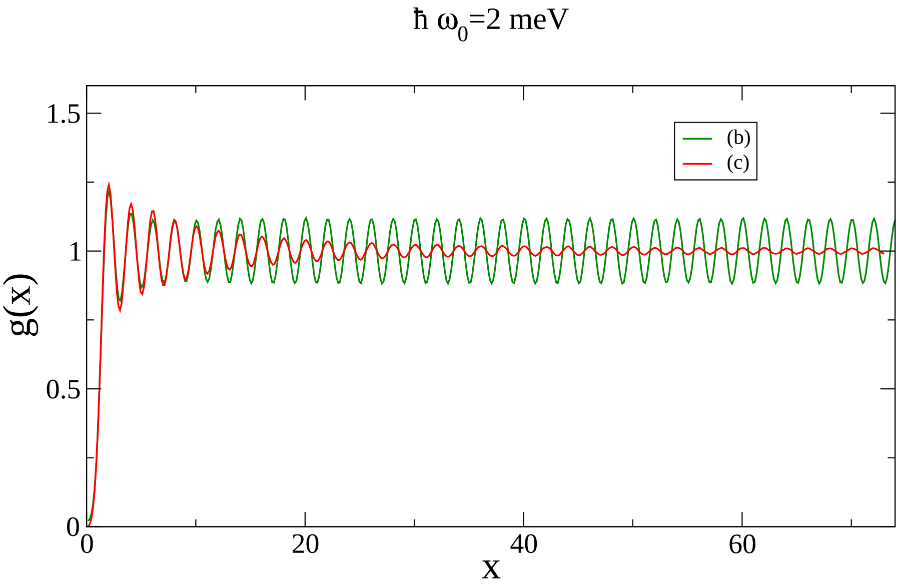

Figure 4.14: Pair correlation function for $r_s = 5$ at $\hbar\omega_0 = 2$meV. The points display the $g(x)$ computed with the polarized liquid (c) and unpolarized solid (b) wavefunction.

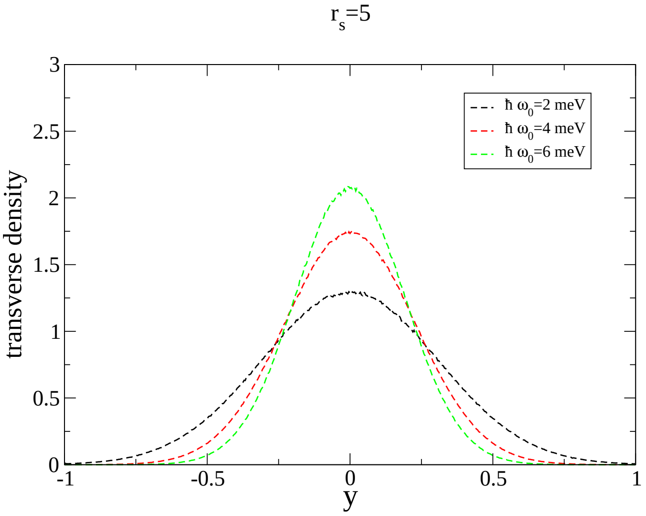

Figure 4.15: Transverse density in the confined 2D electrons gas for $r_s = 5$.

# Chapter 5

# Fermionic Shadow Wave Function

The Shadow Wave Function is a wavefunction used in variational calculations. Its main feature is the capability of describing a quantum system in which inhomogeneities are present (such as a solid perfect of defective, a cluster, a surface) though being written as manifestly translationally invariant function. The system breaking is obtained by the variational minimization of the wavefunction parameters. In the following sections we will give a short overview of the SWF, and develop its application to a many-fermion system.

## 5.1 Shadow Wave Function

The general form of the SWF for symmetric systems is the following:

$$\psi_{SWF}(\mathbf{R}) = \phi_p(\mathbf{R}) \int \Xi(\mathbf{R},\mathbf{S})\phi_s(\mathbf{S})d\mathbf{S}\,, \tag{5.1}$$

where $\mathbf{R} = \{\mathbf{r_1}...\mathbf{r_N}\}$ are the coordinates of the particles and $\mathbf{S} = \{\mathbf{s_1}...\mathbf{s_N}\}$ are the coordinates of auxiliary degree of freedom, *shadows*. $\phi_p$ and $\phi_s$ are Jastrow factors for particles and shadows, respectively,

$$\phi_p(\mathbf{R}) = exp\left[-\sum_{i<j} u_{pp}(\mathbf{r}_{ij})\right] \tag{5.2}$$

$$\phi_s(\mathbf{S}) = exp\left[-\sum_{i<j} u_{ss}(\mathbf{s}_{ij})\right] \tag{5.3}$$

and $\Xi(\mathbf{R},\mathbf{S})$ is a kernel describing the correlations between particles and shadows

$$\Xi(\mathbf{R},\mathbf{S}) = exp\left[-\sum_{i=1}^{N} u_{ps}(|\mathbf{r}_i - \mathbf{s}_i|)\right] \tag{5.4}$$

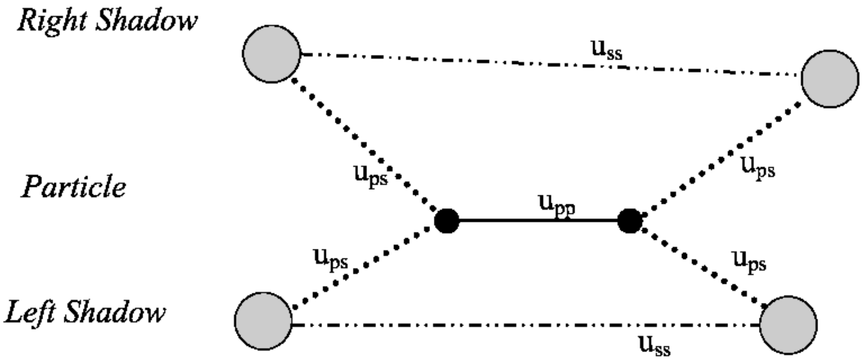

Figure 5.1: Diagram illustrating interaction between trimers: the quantum system is formally equivalent to a classical system of triatomic molecules interacting according this schema

Generally the kernel is formed by a product of Gaussian centered on the shadow positions:

$$\Xi(\mathbf{R},\mathbf{S}) = exp\left[-\sum_{i=1}^{N} c(\mathbf{r}_i - \mathbf{s}_i)^2\right]. \tag{5.5}$$

The Jastrow factors introduce explicit particle–particle and shadow–shadow correlations. The kernel connects particles and shadows.

The estimation of the mean value of operator $\hat{O}$ using SWF in VMC calculation is defined in the following way

$$\langle\hat{O}\rangle_\psi = \frac{\int \psi^*(\mathbf{R})\hat{O}\psi(\mathbf{R})d\mathbf{R}}{\int |\psi^2(\mathbf{R})|d\mathbf{R}} = \frac{\int \psi^*(\mathbf{R})\psi(\mathbf{R})\left[\frac{\hat{O}\psi(\mathbf{R})}{\psi(\mathbf{R})}\right]d\mathbf{R}}{\int |\psi^2(\mathbf{R})|d\mathbf{R}} \quad . \tag{5.6}$$

where

$$\int \psi^*(\mathbf{R})\psi(\mathbf{R})\left[\frac{\hat{O}\psi(\mathbf{R})}{\psi(\mathbf{R})}\right]d\mathbf{R} = \tag{5.7}$$

$$\frac{1}{2}\int\int\int d\mathbf{R}d\mathbf{S}d\mathbf{S}'\left[\hat{O}_{loc}(\mathbf{R},\mathbf{S}) + \hat{O}_{loc}(\mathbf{R},\mathbf{S}')\right]$$

$$\phi_p^2(\mathbf{R})\Xi(\mathbf{R},\mathbf{S})\Xi(\mathbf{R},\mathbf{S'})\phi_s(\mathbf{S})\phi_s(\mathbf{S'})$$

In this equation each particle $\mathbf{r}_i$ is linked to two shadows, $\mathbf{s}_i$ and $\mathbf{s}'_i$, making a trimer (see figure 5.1). The trimers are correlated by Jastrow factors. The integration over the shadow variables introduces then higher-order correlations between particles (see figure 5.1).

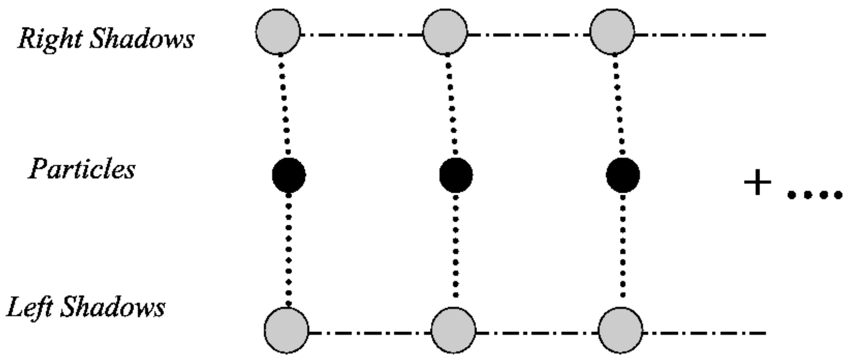

Figure 5.2: Many-body correlation in SWF

In dealing with fermionic systems, one can consider antisymmetric generalizations of the SWF. This can be done in two distinct ways, as described below.

## 5.2 Antisymmetric Shadow Wave Function

The easiest way in order to antisymmetrize SWF is to write a SWF which is antisymmetric with respect to the exchange of the real degrees of freedom. This can be obtained by multiplying the SWF by a product of two determinants, one including the particles with spin up and the other the particles with spin down. The antisymmetric shadow wave function (ASWF) is defined in the following way:

$$\begin{aligned}\psi_{ASWF}(\mathbf{R}) &= \prod_{l=\uparrow,\downarrow} D_l[\phi_k(\mathbf{r}_i)]\phi_p(\mathbf{R}) \\ &\times \int \exp(-c(\mathbf{R}-\mathbf{S})^2)\phi_s(\mathbf{S})d\mathbf{S}\,, \end{aligned} \tag{5.8}$$

where $D_l$ are the determinants, $l$ is the spin, and the $\{\phi_k(\mathbf{r}_i)\}$ are the single particle basis functions, usually taken as plane waves satisfying Born–von Karman periodic boundary conditions, possibly including backflow correlations.

Using $\psi_{ASWF}(\mathbf{R})$ it is possible to obtain good results. In fact, $\psi_{ASWF}(\mathbf{R})$ was successfully applied to study the ground state properties of liquid and solid $^3$He [35] and two–dimensional electron gas [61].

The strong limit of ASWF is that the auxiliary degrees of freedom are not antisymmetrized. In the next section we display the advantage of imposing the antisymmetry on the auxiliary degrees of freedom.

## 5.3 Fermionic Shadow Wave Function

There is another way of antisymmetrizing a SWF. This method is computationally more expensive but it presents some advantages. This form, called Fermionic Shadow Wave Function (FSWF) is built by imposing the antisymmetry on the auxiliary degrees of freedom rather than on the real ones:

$$\begin{aligned}&\psi_{FSWF}(\mathbf{R}) = \\ &\phi_p(\mathbf{R}) \int \exp(-c(\mathbf{R}-\mathbf{S})^2) \prod_{l=\uparrow,\downarrow} D_l[\phi_k(\mathbf{s}_i)]\phi_s(\mathbf{S})d\mathbf{S}\,. \end{aligned} \tag{5.9}$$

It is possible to show that $\psi_{FSWF}$ is antisymmetric under the exchange of two particles of like spin [62]. Let $P$ be a permutation. Defining:

$$S^* = P^{-1}S; \qquad D(S) = D_\uparrow[\phi_k(\mathbf{s}_i)]D_\downarrow[\phi_k(\mathbf{s}_i)],$$

one can show that the following tree properties hold:

$$(PR-PS^*)^2 = (R-S)^2; \quad D(PS^*) = (-1)^P D(S^*);$$

$$d(PS^*) = dS^*; \quad \phi_x(PX) = \phi_x(X)$$

where $\phi_x$ are the Jastrow factors, from which follows:

$$\begin{aligned}\psi_{FSWF}(PR) &= \phi_p(PR)\int e^{-c(PR-S)^2}D(S)\phi_s(S)dS \qquad (5.10)\\ &= \phi_p(PR)\int e^{-c(PR-PS^*)^2}D(PS^*)\phi_s(PS^*)dS^* \\ &= (-1)^P\phi_p(R)\int e^{-c(R-S^*)^2}D(S^*)\phi_s(S^*)dS^* \\ &= (-1)^P\psi_{FSWF}(R)\end{aligned}$$

Equation 5.9 is just the simplest version of FSWF. It will become evident later it is convenient to sum over all the possible permutations of shadows. This is easily obtained. In fact using the fact that $S$ are integration variables, it is possible permute their indices and obtain a new form of FSWF:

$$\begin{aligned}&\psi_{FSWF}(\mathbf{R}) = \\ &\phi_p(\mathbf{R})\int \prod_{l=\uparrow,\downarrow} D_l\left[\exp(-c|\mathbf{r}_\alpha - \mathbf{s}_\beta|^2)\right] \prod_{l=\uparrow,\downarrow} D_l[\phi_k(\mathbf{s}_i)]\phi_s(\mathbf{S})d\mathbf{S}\end{aligned} \tag{5.11}$$

This is the form that will be used in the following.

Observing the equation 5.11 it is clear the nodal structure is described by a product of two determinants, both defined over the auxiliary degrees of freedom. In this way the nodal surface is not defined *a priori*.

Further, in the strong localization regime this function 5.11 becomes very close to an antisymmetrized Nosanow-Jastrow wavefunction. Instead at low densities the nodal structure is comparable to that of a determinant of plane waves, but with the inclusion of correlations at any order due to the integration on the shadow variable.

Now it is clear how in $\psi_{FSWF}(\mathbf{R})$ the thermodynamic phase emerges implicitly in the variational optimization and how it is possible to reproduce a good nodal surface.

### 5.3.1 FSWF problems

The evaluation of the integral 5.7 present a serious sign problem that plagues the implementation when FSWF is used. In VMC the square of the wavefunction is used as a probability density, $P(\mathbf{R})$, and the local energy is averaged over the sampled configurations. Thus

$$E = \frac{\int d\mathbf{R}\psi^*(\mathbf{R})\psi(\mathbf{R})E_L}{\int d\mathbf{R}\psi^*(\mathbf{R})\psi(\mathbf{R})} = \frac{\int d\mathbf{R}P(\mathbf{R})E_L}{\int d\mathbf{R}P(\mathbf{R})}\,, \tag{5.12}$$

where $E_L = \psi^{-1}H\psi$ is the local energy of the system. The integral is evaluated by generating configurations according to $P = |\psi|^2$ that are sampled using the Metropolis algorithm.

When using SWF, one constructs $\psi^*(\mathbf{R})\psi(\mathbf{R})$ by integrating over two sets of shadow variables, $\mathbf{S}, \mathbf{S}'$. Choosing some probability density function, $P(\mathbf{R}, \mathbf{S}, \mathbf{S}')$, and sampling it in the usual way, a generic operator can be computed as

$$\langle O \rangle = \frac{\int d\mathbf{R}d\mathbf{S}d\mathbf{S}'\tilde{P}(\mathbf{R}, \mathbf{S}, \mathbf{S}')w(\mathbf{R}, \mathbf{S}, \mathbf{S}')O(\mathbf{R})}{\int d\mathbf{R}d\mathbf{S}d\mathbf{S}'\tilde{P}(\mathbf{R}, \mathbf{S}, \mathbf{S}')w(\mathbf{R}, \mathbf{S}, \mathbf{S}')}\,. \tag{5.13}$$

A reasonable choice for ordinary SWF is simply the integrand:

$$\begin{aligned} &P(\mathbf{R}, \mathbf{S}, \mathbf{S}') = \phi_p^2(\mathbf{R}) \\ &\times \exp(-c(\mathbf{R}-\mathbf{S})^2 - c(\mathbf{R}-\mathbf{S}')^2)\phi_s(\mathbf{S})\phi_s(\mathbf{S}')\,, \end{aligned} \tag{5.14}$$

with $w = 1$. Similarly in $\psi_{ASWF}$ the integrand is positive definite, and can be used for $P(\mathbf{R}, \mathbf{S}, \mathbf{S}')$.

When one uses $\psi_{FSWF}$, the integrand is not everywhere positive. In this case, a practical sampling function is the absolute value of the integrand. Let

$$\begin{aligned} Q(\mathbf{R},\mathbf{S},\mathbf{S}') &= \phi_p^2(\mathbf{R}) \prod_{l=\uparrow,\downarrow} D_l \left[\exp(-c|\mathbf{r}_\alpha - \mathbf{s}_\beta|^2)\right] \prod_{l=\uparrow,\downarrow} D_l \left[\exp(-c|\mathbf{r}_\alpha - \mathbf{s}'_\beta|^2)\right] \\ &\quad \times \prod_{l=\uparrow,\downarrow} D_l[\phi_k(\mathbf{s}_i)] \prod_{l'=\uparrow,\downarrow} D_{l'}[\phi_k(\mathbf{s}'_i)]\phi_s(\mathbf{S})\phi_s(\mathbf{S}') \,, \qquad (5.15) \\ \tilde{P}(\mathbf{R},\mathbf{S},\mathbf{S}') &= |Q(\mathbf{R},\mathbf{S},\mathbf{S}')| \,, \qquad (5.16) \\ w(\mathbf{R},\mathbf{S},\mathbf{S}') &= \frac{Q(\mathbf{R},\mathbf{S},\mathbf{S}')}{|Q(\mathbf{R},\mathbf{S},\mathbf{S}')|} \equiv \pm 1 \,. \qquad (5.17) \end{aligned}$$

Averaging over estimates of different signs presents a challenge. Numerical experiment shows that for large systems, convergence to acceptable statistical errors is very slow. This is particularly true for disordered systems. Of course, the average of $|\psi_{FSWF}|^2$ is positive, and the variance exists, so that the sign problem is not intractable.

### 5.3.2 Proposed solution to FSWF sign problem

A simple reorganization of the calculation, however, produced a dramatic improvement in the Monte Carlo efficiency. In applying the Metropolis method to shadow wavefunction, including the ASWF variant, the usual procedure is to sample new values of $\mathbf{R}$, $\mathbf{S}$, and $\mathbf{S}'$ in turn. It is always true that the integrals in Eq. (5.13) over $\mathbf{S}$ and $\mathbf{S}'$ for fixed $\mathbf{R}$ are positive. This suggests that a change in the order of summation might be useful for the FSWF class of functions, especially with disorder, by propagating the shadows **S** and **S'** for $M$ steps (with $M$ big enough) for fixed $\mathbf{R}$. That is, we expect that the sum of the ±1–weight of $M$ steps

$$\left[\sum w_i\right]_S \times \left[\sum w_i\right]_{S'} = W_S W_{S'} \,, \qquad (5.18)$$

will be usually positive. In fact, increasing $M$ in the more difficult cases where exchanges of sign often appear, gives weights $W_S W_{S'}$ positive and significantly different from zero. The algorithm becomes: i) sample a configuration $\mathbf{R}$ of particles, ii) sample $M$ configurations of $\mathbf{S}$, iii) sample $M$ configurations of $\mathbf{S}'$, iv) combine all the weight factors and accumulate the local energy for the average and variance, iterate from i) to iv) until the convergence is reached and the variance is low as desired.

$M$ is the number of steps to be used in order to compute the integral over the shadow variables. It is very important to choose carefully the value of $M$. $M$ has to be large enough to guarantee that the integral reach convergence. But if $M$ is too large the computational time increases too much. So it is necessary to find a good compromise in the value of $M$. This observation clarifies the limits of this method. The efficiency will be largely improved for systems in which the sign is not so severe (as solid $^3$He), while the improvement is not definitive for low-density disordered systems (liquid $^3$He, electron gas).

In a perfect $^3$He crystal it is possible to perform the calculations using $M = 1$. Instead when a vacancy is added it is necessary to use $M$ as larger as $1.5 \times 10^3$. In liquid the value of $M$ should be further increased.

## 5.4 Ground state properties of $^3$He vacancies

As an illustration of the power of FSWF, we studied the ground state of the solid $^3$He in the range of molar volumes between 20 and 24 cc/mol and we compare the results with to the previous variational estimates based on antisymmetric functions. As a next step, we studied the vacancy formation energy by computing the energy in the presence of an empty site. We stress the fact that it is not possible to study an antisymmetric system with disorder using DMC or GFMC methods due to the limits imposed by a preventive choice of the single particle functions used to build the Slater determinant of the importance function.

### 5.4.1 Technical details

In the Hamiltonian of the system

$$H = -\frac{\hbar^2}{2m}\sum_i \nabla_i^2 + \sum_{i<j} V(r_{ij}) \tag{5.19}$$

the He–He interaction is the Hartree-Fock dispersion HFDHE2 potential by Aziz *et al.* [63]:

$$\begin{aligned} V(r) &= \epsilon V^*(x) \qquad (5.20)\\ V^*(x) &= Ae^{-\alpha x} - \left\{ \frac{C_6}{x^6} + \frac{C_8}{x^8} + \frac{C_{10}}{x^{10}} \right\} F(x) \end{aligned}$$

where $x = r/r_m$ and $F(x)$ is defined in the following way

$$\begin{aligned} F(x) = exp\left\{ -\left[\frac{D}{x} - 1\right]^2 \right\} & \qquad \text{for} \quad x < D \\ = 1 & \qquad \text{for} \quad x \geq D \end{aligned}$$

In table 5.1 there are the potential coefficients.

In the FSWF the particle Jastrow factor $\phi_p(R)$ is

$$\phi_p(R) = \prod_{i<j} e^{-\frac{1}{2}u(r_{ij})} \tag{5.21}$$

| | |
|---|---|
| $C_6$ | 1.3732412 |
| $C_8$ | 0.4253785 |
| $C_{10}$ | 0.178100 |
| $A$ | 0.5448504 |
| $\alpha$ | 13.353384 |
| $D$ | 1.241314 |
| $r_m$ | 2.9673 (Å) |
| $\epsilon$ | 10.8 (K) |

Table 5.1: Reduced parameters for the HFDHE2 potential.

where as pseudo-potential $u(r_{jl})$ we used a McMillan form[35] combined with a summation over a basis as in Ref. [64]:

$$u(r_{ij}) = u^0(r_{ij}) + \sum_m a_m \chi_m(r_{ij}) \tag{5.22}$$

the terms are explicitly

$$u^0(r) = \left(\frac{b}{r}\right)^5$$

$$\begin{aligned}\chi_m(r) &= \left[1 - cos\left(\frac{2\pi m}{L - 2r_c}(r - L/2)\right)\right] r^n \qquad && (r > r_c)\\ &= r^n && (r < r_c)\end{aligned}$$

where $L$ is side of the simulation box.

In the Jastrow factor $\phi_s$ the pseudo-potential is defined as the rescaled interaction $u_s(r_{ij}) = c_1 V(c_2 r_{ij})$ ($c_1$ and $c_2$ are additional variational parameters).

All the variational parameters entering in the wavefunction were optimized at each density using an energy–variance minimization technique due to C.J. Umrigar and M.P Nightingale applied to the system with no defects.

### Vacancy formation energy

The vacancy formation energy at constant pressure for a system with $N$ particles at a fixed density $\rho$ can be estimated as

$$\Delta E_v = E(N-1, N_l = N) - \frac{N-1}{N} E(N, N_l = N)\,, \tag{5.23}$$

where the number of lattice sites $N_l$ is conserved and the density of the two systems is the same. The vacancy formation energy includes contributions from lattice relaxation and tunneling that cannot be accounted for by a wavefunction with an underlying lattice structure (such as a Nosanow–like wavefunction). The computation of the energy for the system with $N-1$ particles is performed by removing one particle and one shadow from the trial wavefunction. It has to be noted that by dropping one shadow from the shadow determinant means having a hole–state in one of the determinants of Eq. 5.9. In the case of open–shell configuration where one or more single particle states are not filled one needs to perform the calculation using twist average boundary conditions [65], so that the total wavefunction has zero total momentum. In the case of FSWF, we conjecture that it is not important which particular shadow orbital is omitted, because the total momentum of the system is always conserved.

We tested our conjecture by repeating the same calculation removing different single shadow states from the kernel. In particular the energy of the system where orbitals with different vector number $\mathbf{n}$ were removed is the same within statistical error. We stress that by contrast, in using a normal many–body wavefunction with no shadows or using ASWF the energy would depend upon the unfilled single–particle orbital.

### 5.4.2 Results

We report the energy of 54 atoms in table 5.2. The energy per particle is also displayed in Fig. 5.3 where we compared our results (circles) with those found in Ref. [35] computed using ASWF starting from a normal antiferromagnetic order NAF (diamonds), and including exchanges (triangles), and with the more accurate DMC of Ref. [66] (squares). As can be seen FSWF provides lower variational estimates of the energy. The DMC energies are lower at each density by a constant value of about 1K.

| $\rho\sigma^3$ | E/N(54) | T/N(54) |
|---|---|---|
| 0.419 | 0.422(1) | 23.947(1) |
| 0.427 | 0.548(2) | 24.608(1) |
| 0.438 | 0.955(1) | 26.005(2) |
| 0.457 | 1.556(1) | 27.986(2) |
| 0.479 | 2.455(1) | 30.482(2) |
| 0.503 | 3.481(1) | 32.487(2) |

Table 5.2: Total and kinetic energy per particle at different densities in the solid b.c.c. phase for the crystal with no defects (54 atoms). All energies are expressed in $K$.

The energies of the system with a vacancy are reported in table 5.3. The vacancy formation energy obtained by Eq. 5.23 as a function of the density

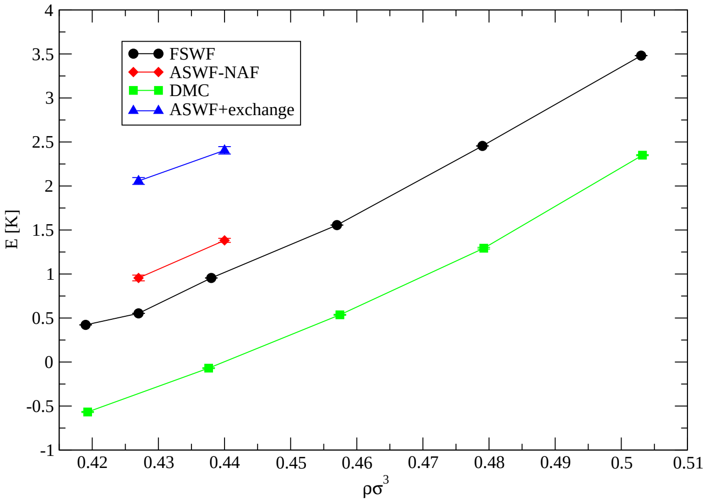

Figure 5.3: The FSWF energy per particle (black circles) as a function of the density. The result is compared with the two results provided by ASWF of Ref. [35] (blue triangles and red diamonds) and with the DMC results of Ref. [66].

is given in Fig. 5.4, where we included the same calculation using the static shadows (red points).

We assume that the system containing one empty site is well described by the same wavefunction of the perfect crystal. The modified structure of the system with a vacancy is modeled by the shadow variables. Therefore for 53 atoms we used the same parametrization of $\phi_p$, $\phi_s$ and the coupling constant $c$ entering in Gaussians of the system with 54 atoms.

In the static shadow case the shadow degrees of freedom are kept fixed on the lattice sites so their effect is switched off. This corresponds to using a variational wavefunction of the antisymmetric Jastrow–Nosanow type. FSWF is more effective clearly shown in the figure. The vacancy formation energy computed by means of FSWF is larger than the experimental data (blue points) taken from Ref. [67] (see also Ref. [68] and references therein). The discrepancy can be attribute to several reasons. First of all the calculation might be affected by strong finite size effects. In fact the effective concentration of vacancies in the system is rather high (i.e. 1/N), and this might imply a contribution to the vacancy formation energy coming from a vacancy-vacancy interaction. There is also additional room for improvement in the overall variational description. For example, the parameters could be re-optimized in presence of the vacancy, or a more sophisticated version of the wavefunction including a local–density dependence of the two–body correlations might be used[36].

| $\rho\sigma^3$ | E/N(53) | T/N(53) |
|---|---|---|
| 0.419 | 0.69(1) | 23.71(3) |
| 0.427 | 0.78(8) | 24.6(2) |
| 0.438 | 1.26(1) | 25.76(3) |
| 0.457 | 1.844(8) | 28.05(2) |
| 0.479 | 2.801(7) | 30.60(2) |
| 0.503 | 4.127(7) | 32.35(2) |

Table 5.3: Total and kinetic energy per particle at different densities in the solid b.c.c. phase for the crystal with the presence of an empty site (53 atoms). All energies are expressed in $K$.

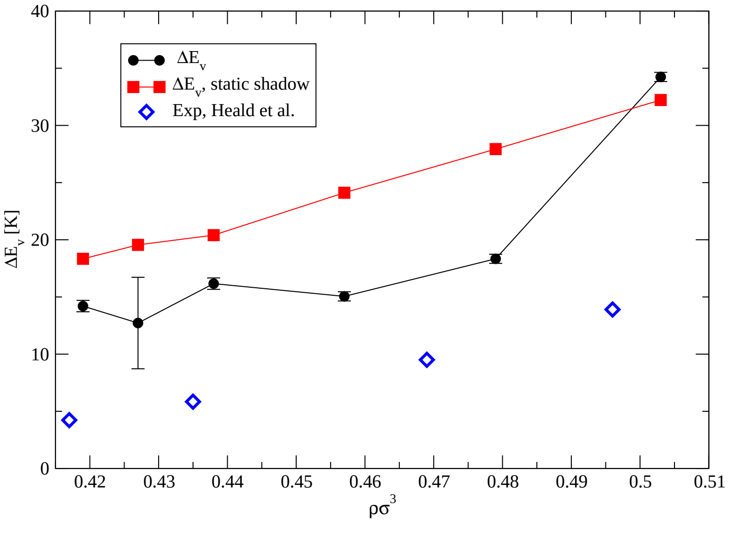

Figure 5.4: The vacancy formation energy $\Delta E_v$ as a function of the density using the FSWF (black points) and by keeping the shadows fixed. Some experimental data from Ref. [67] is also reported for comparison. See the text for details.

In figure 5.5 we show the cumulative normalization factor of the probability density function $\Xi_{FSWF}$. This quantity tends to have wide oscillation due to the contribution of positive and negative terms. With the new method this quantity tends to converges to a small but positive costant value.

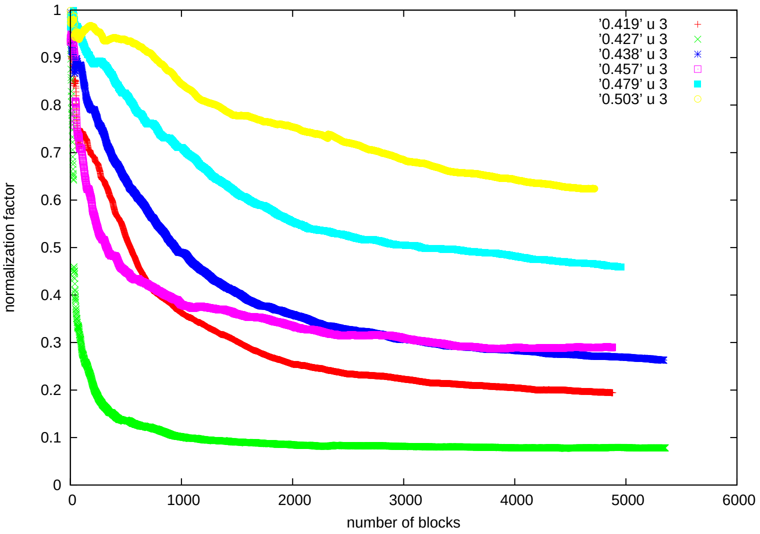

Figure 5.5: Normalization factor of the FSWF (Denominator of equation 5.13), for different values of density. Note the exponential decay and the asymptotic limit that is always greater than zero.

We also computed the particle–particle and shadow–shadow pair distribution functions for pairs with parallel and opposite spin at different densities. Results are reported in Fig. [5.6-5.9]. It is possible to note a typical feature of SWF calculations in crystal, i.e. the shadows are more localized than particles. Further increasing the density, the system results more localized. The vacancy introduces disorder. In the pair distribution functions with parallel spins the system displays a tendency of organizing itself in a hybrid spin ordering, possibly suggesting the formation of the experimentally observed $u2d2$ magnetic ordering. This would be a sign that magnetic ordering in $^3$He crystals strongly depends on the detailed character of the interaction.

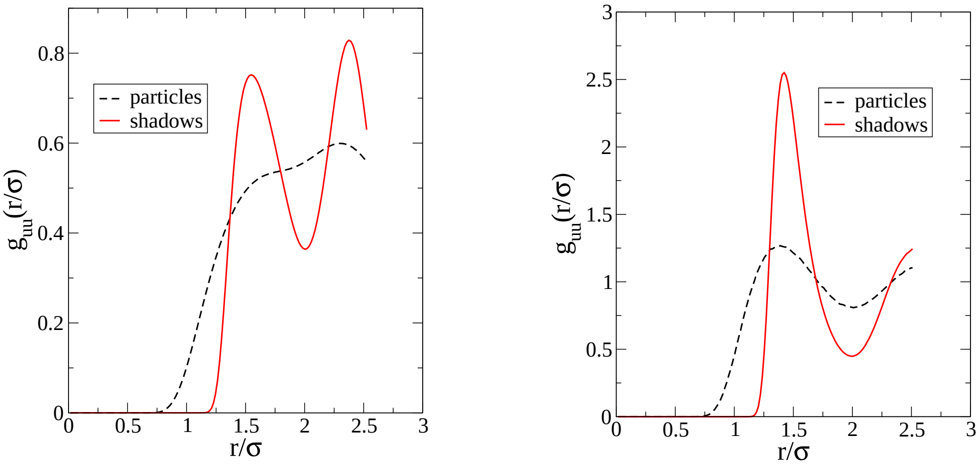

Figure 5.6: Pair distribution functions for two $^3$He atoms with parallel spins for N=54 and N=53 at 20 cc/mol. Distance is given in units of $\sigma = 2.556$Å.

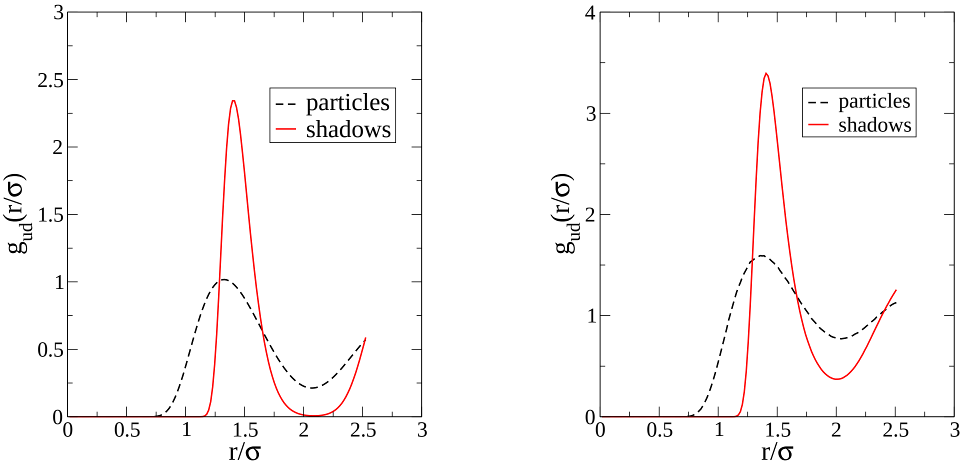

Figure 5.7: Pair distribution functions for two $^3$He atoms with opposite spins for N=54 and N=53 at 20 cc/mol. Distance is given in units of $\sigma = 2.556$Å.

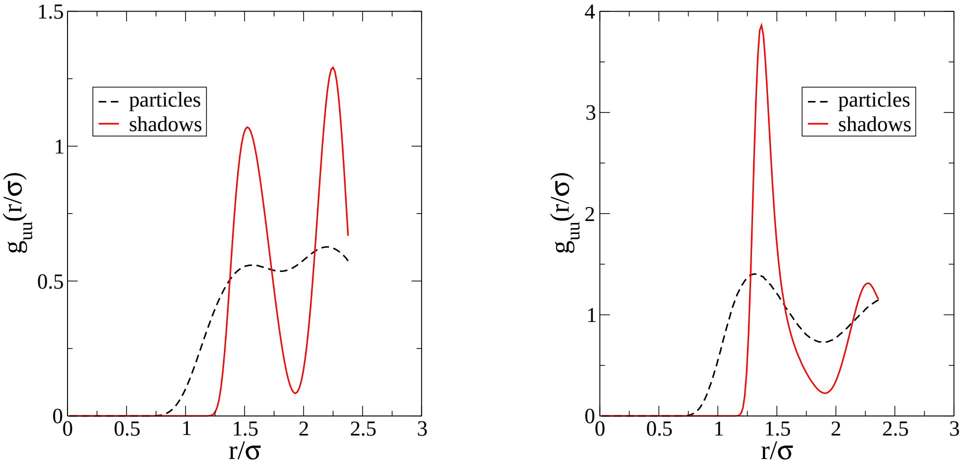

Figure 5.8: Pair distribution functions for two $^3$He atoms with parallel spins for N=54 and N=53 at 24 cc/mol. Distance is given in units of $\sigma = 2.556$Å.

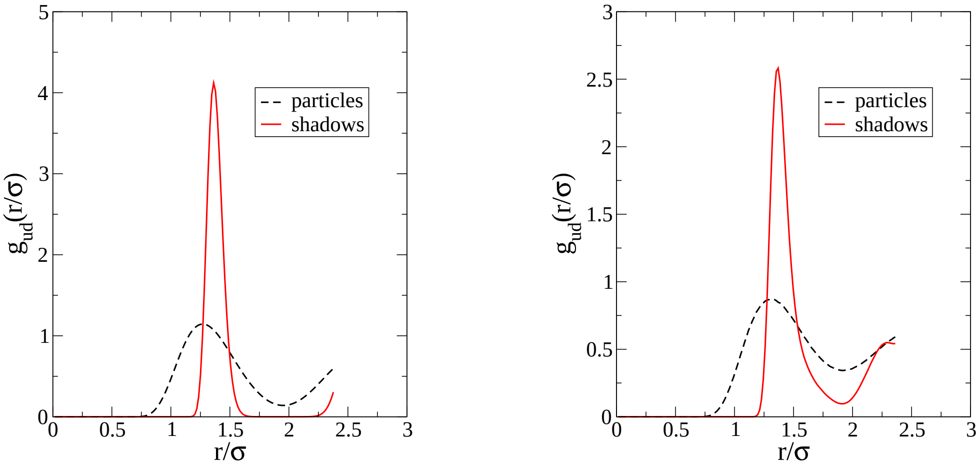

Figure 5.9: Pair distribution functions for two $^3$He atoms with opposite spins for N=54 and N=53 at 24 cc/mol. Distance is given in units of $\sigma = 2.556$Å.

# Chapter 6

# Conclusions and perspectives

This thesis work was concerned in the attempt of improving two Quantum Monte Carlo methods, VMC and DMC, in order to extend the technical capabilities to the treatment of strongly inhomogeneous and strongly correlated Fermions. Such system have been posing a technical challenge for many years, and a general method that includes a correct treatment of the symmetry properties and guarantees a satisfactory computational efficiency is still lacking. We focused our attention on two particular cases.

In the first project we performed a Diffusion Monte Carlo simulation of a 2D electron gas laterally confined by harmonic potential. This model is of great interest because contrarily to quasi 1D models we can study the occurrence of phase transitions relevant for understanding the anomalies observed in the conductance of quantum nano-wires.

We studied in detail the cases with $\hbar\omega_0$ =2,4,6 meV, where $\omega_0$ is the parameter of the confinement. Comparing the results we can say the system is a polarized and localized at $r_s > 3$ and unpolarized liquid at $r_s < 3$. Increasing $\omega_0$ the system tends to become more localized, but at high density it is difficult to turn off the electron exchange.

It is necessary to have a complete overview of all results on this system in order to be able to give an interpretation. The computational difficulties are not negligible. The presence of the lateral confinement induces correlations that may give rise to unconventional structures for the ground state. In particular, using a wavefunction built starting from localized orbitals gives in some case the lowest energy, despite high mobility due to the exchange among electrons does not allow to speak about a crystal phase. This behavior might suggest the presence of a spin-wave ground state. On the other hand the lateral confinement tends to induce a localization (visible on the two body density) also when plane waves are used to build the wavefunction.

It is clear for $r_s \geq 5$ the polarized liquid wavefunction reproduce in a better way the nodal structure giving the smallest energy. But at $r_s \geq 5$ is the system still liquid or not? A better energy can be obtained by using a polarized liquid wavefunction instead of a polarized solid wavefunction, but the pseudo-solid structure of $g(x)$ computed using the polarized liquid wavefunction indicates us the existence of a localization. We think that for $r_s \geq 5$ the system is polarized and weak localized.

For $r_s < 3$ the system is always liquid. As $\hbar\omega_0 = 6$ meV the unpolarized solid wavefunction can give a lower energy than unpolarized liquid wave, but the electron exchange guarantees the liquid behavior of the system. There are some indications concerning the formation of a spin wave at $r_s = 1$.

In conclusion the study of the laterally confined electron gas would require an even more detailed analysis in order to completely determine the phase diagram.

The next step will be the study of system at even higher values of $\omega_0$. In the limit of very strong confinement the system should become effectively 1D. It is known that in this regime a transition to a Luttinger liquid is possible. One interesting signature of this transition would be the equivalence of the energy of the Fermion and Boson systems. We expect the system tends to a localized configuration in which the Fermionic contribution to energy is negligible. To realized that is necessary to make some small changes in the current version of the code.

Other important developments concern to reproduce more accurately the experimental setup, for example, introducing a spin-orbit term (that comes from the presence of an electronic field transverse to the quantum well), and a magnetic field.

In the second project we present a novel variational wavefunction to study Fermionic systems with the presence of defects and in general in a inhomogeneous phase. As an application we described the Fermionic Shadow wave function that we used to compute the equation of state of solid $^3$He in the b.c.c. phase as a function of the density, and the vacancy formation energy.

We stress the fact that using the standard QMC machineries it is not possible to correctly study systems with the presence of defects or impurities like a vacancy. In particular the theoretical study of $^3$He with vacancies is a problem that has not been well solved yet, and no other convincing ab-initio theories are present.

Using FSWF it is possible to study the $^3$He with the presence of impurities of $^4$He as well as the mixture of the two gases, and to move near the region where the solid and liquid phases start to coexist. Work in these directions is in progress.

FSWF would find an interesting application to other systems, for example the electron gas. The extension to other systems might not be simple. In fact, some checks on two-dimensional electron gas showed us our model does not always work so good. The electron system is more difficult than $^3$He because of the lighter mass and higher delocalisation. However, the goal of using FSWF in this case might be a breakthrough in the theoretical description of the properties of the quantum wells in presence of charge impurities, that would be of great interest for experiments and applications.

# Acknowledgements

Questa tesi è dedicata a Pradiip, senza il suo costante appoggio probabilmente non l'avrei portata a termine.

Ringrazio Francesco Pederiva che mi ha dato la possibilità di fare questa esperienza e che non ha mai smesso di scommettere su di me. Ringrazio Enrico Lipparini che con il suo modo diretto di esprimersi è stato spesso risolutivo nelle decisioni importanti.

Ringrazio tutti i miei colleghi.

- Grazie Michele di aver condiviso con me ogni attimo di questa esperienza, dal corridoio all'ufficio la stessa fortuna e la stessa sorte.
- Grazie Sebastiano, nostro rappresentante e saggio consigliere. Grazie per ogni volta che mi hai ascoltato.
- Grazie Stefano per la tua gentilezza, disponibilità e pazienza!
- Grazie Alberto per la tua compagnia. Sarà difficile dimenticare il tuo entusiasmo all'aeroporto di Helsinki!
- Grazie Paolo, sempre disposto a dare una mano e qualche buon consiglio.

Concludo ringraziando la mia famiglia, eterno punto di riferimento.

# List of Figures

1.1 Energy Band of basic high-electron-mobility-transistors (HEMT). 2

1.2 A one dimensional quantum wire realized at the edge of a two dimensional electron gas [1] . . . . . . . . . . . . . . . . . . . . . 3

1.3 (left) Schematic of a split-gate device, where S and D represent the source and drain contacts [2]. (Right) Gate configuration used to define the wire. The top gate and side gates are separately adjusted to control the electron density and the wire confinement potential [3]. . . . . . . . . . . . . . . . . . . . . . . . . . . . . 4

1.4 Experimental result[7]. Conductance of a $l = 0.5\mu$m quantum wire as a function of side gate voltage for $V_T$ =560 mV-1500 mV (right to left). Inset: Conductance as a function of side gate voltage for $V_T$=1.5 V . . . . . . . . . . . . . . . . . . . . . 5

1.5 Phase diagram of $^3$He below 3 mK. The solid phase appears only above the pressure of 34 bar. At high temperatures the liquid is in the normal Fermi state. There are two superfluid phases, A and B. . . . . . . . . . . . . . . . . . . . . . . . . . . . . 7

4.1 Total energy per electron (in effective Rydberg) for a laterally confined two dimensional electron gas. Dots: unpolarized fluid; triangles: unpolarized crystal; squares: polarized fluid; diamonds: polarized crystal. The full line is the energy of the 2D system at a value of $r_s^{2D}$ estimated from the width of the lateral density of electrons. We report also an estimation of energy at $r_s = 0.25$. . 31

4.2 QMC diffusion of the electrons in the wire (in units of $a_0^*$) as a function of $r_s$ at $\hbar\omega_0 = 4$meV. The points display the computed diffusion for the unpolarized liquid (dots), polarized liquid (squares), localized (triangles) and polarized solid (diamonds) phases. . . . . . . . . . . . . . . . . . . . . . . . . . . . . 32

4.3 Electron displacements in liquid phase at low density ($r_s = 5$) for pair of electrons with opposite spin (top) and with same spin (bottom) . . . . . . . . . . . . . . . . . . . . . . . . . . . . 33

4.4 Transverse density in the confined 2D electrons gas. The density computed by DMC is compared with the "jellium" density, i.e. from the density given by the ground state solution of the confining harmonic potential. Curves are given for $r_s = 1$ (dotted and dashed-dotted line), and $r_s = 5$ (full and dashed lines). $y$ is given in units of $a_0^*$ . . . . . . . . . . . . . . . . . . . . . . . . . . 34
4.5 Pair correlation function for $r_s = 1$ and $r_s = 5$. . . . . . . . . . . 35
4.6 Spin density function for $r_s = 1$ and $r_s = 5$. . . . . . . . . . . 35
4.7 QMC diffusion of the electrons in the wire (in units of $a_0^*$) as a function of $r_s$ at $\hbar\omega_0 = 6$meV. The points display the computed diffusion for the unpolarized liquid (dots), polarized liquid (squares), localized (triangles) and polarized solid (diamonds) phases. . . . . . . . . . . . . . . . . . . . . . . . . . . . . 37
4.8 Pair correlation function for $r_s = 1$ at $\hbar\omega_0 = 6$meV. The points display the $g(x)$ computed with the unpolarized liquid (a) and solid (b) wavefunction. . . . . . . . . . . . . . . . . . . . . . 38
4.9 Pair correlation function for $r_s = 3$ at $\hbar\omega_0 = 6$meV. The points display the $g(x)$ computed with the unpolarized liquid (a) and solid (b) wavefunction. . . . . . . . . . . . . . . . . . . . . . 39
4.10 QMC diffusion of the electrons in the wire (in units of $a_0^*$) as a function of $r_s$ at $\hbar\omega_0 = 2$meV. The points display the computed diffusion for the unpolarized liquid (dots), polarized liquid (squares), localized (triangles) and polarized solid (diamonds) phases. . . . . . . . . . . . . . . . . . . . . . . . . . . . . 39
4.11 Pair correlation function for $r_s = 3, 5, 7$ at $\hbar\omega_0 = 6$meV. The points display the $g(x)$ computed with the polarized liquid wavefunction. . . . . . . . . . . . . . . . . . . . . . . . . . . . . 40
4.12 Pair correlation function for $r_s = 3, 5, 7$ at $\hbar\omega_0 = 6$meV. The points display the $g(x)$ computed with the unpolarized solid wavefunction. . . . . . . . . . . . . . . . . . . . . . . . . . . . . 41
4.13 Pair correlation function for $r_s = 5$ at $\hbar\omega_0 = 6$meV. The points display the $g(x)$ computed with the polarized liquid (c) and unpolarized solid (b) wavefunction. . . . . . . . . . . . . . . . . . 41
4.14 Pair correlation function for $r_s = 5$ at $\hbar\omega_0 = 2$meV. The points display the $g(x)$ computed with the polarized liquid (c) and unpolarized solid (b) wavefunction. . . . . . . . . . . . . . . . . . 43
4.15 Transverse density in the confined 2D electrons gas for $r_s = 5$. . 43

5.1 Diagram illustrating interaction between trimers: the quantum system is formally equivalent to a classical system of triatomic molecules interacting according this schema . . . . . . . . . . 46
5.2 Many-body correlation in SWF . . . . . . . . . . . . . . . . . 47

5.3 The FSWF energy per particle (black circles) as a function of the density. The result is compared with the two results provided by ASWF of Ref. [35] (blue triangles and red diamonds) and with the DMC results of Ref. [66]. . . . . . . . . . . . . . . . . . . . . 54
5.4 The vacancy formation energy $\Delta E_v$ as a function of the density using the FSWF (black points) and by keeping the shadows fixed. Some experimental data from Ref. [67] is also reported for comparison. See the text for details. . . . . . . . . . . . . . . . . 55
5.5 Normalization factor of the FSWF (Denominator of equation 5.13), for different values of density. Note the exponential decay and the asymptotic limit that is always greater than zero. . . . . 56
5.6 Pair distribution functions for two $^3$He atoms with parallel spins for N=54 and N=53 at 20 cc/mol. Distance is given in units of $\sigma = 2.556$Å. . . . . . . . . . . . . . . . . . . . . . . . . . . 57
5.7 Pair distribution functions for two $^3$He atoms with opposite spins for N=54 and N=53 at 20 cc/mol. Distance is given in units of $\sigma = 2.556$Å. . . . . . . . . . . . . . . . . . . . . . . . . . . 57
5.8 Pair distribution functions for two $^3$He atoms with parallel spins for N=54 and N=53 at 24 cc/mol. Distance is given in units of $\sigma = 2.556$Å. . . . . . . . . . . . . . . . . . . . . . . . . . . 58
5.9 Pair distribution functions for two $^3$He atoms with opposite spins for N=54 and N=53 at 24 cc/mol. Distance is given in units of $\sigma = 2.556$Å. . . . . . . . . . . . . . . . . . . . . . . . . . . 58

# List of Tables

3.1 Differences among wavefunctions (a), (b), (c), (d). $c_2 = \hat{\omega}' + c$. . 19

4.1 Total energy per electron (in effective Rydberg) for a laterally confined two dimensional electron gas with $\hbar\omega_0$=4meV. (a): unpolarized liquid wavefunction. (b): localized wavefunction. (c): polarized liquid wavefunction. (d): polarized solid wavefunction. (*): N=74. . . . . . . . . . . . . . . . . . . . . . . . . . . . . 31
4.2 Total energy per electron (in effective Rydberg) for a laterally confined two dimensional electron gas with $\hbar\omega_0$=2meV. (a): unpolarized liquid wavefunction. (b): localized wavefunction. (c): polarized liquid wavefunction. (d): polarized solid wavefunction. (*): $N = 72$. . . . . . . . . . . . . . . . . . . . . . . . . . . . . 36
4.3 Total energy per electron (in effective Rydberg) for a laterally confined two dimensional electron gas with $\hbar\omega_0$=6meV. (a): unpolarized liquid wavefunction. (b): localized wavefunction. (c): polarized liquid wavefunction. (d): polarized solid wavefunction. 37

5.1 Reduced parameters for the HFDHE2 potential. . . . . . . . . . 52
5.2 Total and kinetic energy per particle at different densities in the solid b.c.c. phase for the crystal with no defects (54 atoms). All energies are expressed in $K$. . . . . . . . . . . . . . . . . . . . . 53
5.3 Total and kinetic energy per particle at different densities in the solid b.c.c. phase for the crystal with the presence of an empty site (53 atoms). All energies are expressed in $K$. . . . . . . . . 55

# Bibliography

[1] A. Yacoby1, H. L. Stormer1, Ned S. Wingreen2, L. N. Pfeiffer1, K. W. Baldwin1, and K. W. West1. Nonuniversal conductance quantization in quantum wires. *Phys. Rev. Lett*, 77:4612, 1996.

[2] K. J. Thomas, J. T. Nicholls, N. J. Appleyard, M. Y. Simmons, M. Pepper, D. R. Mace, W. R. Tribe, and D. A. Ritchie. Interaction effects in a one-dimensional constriction. *Phys. Rev. B*, 58(8):4846–4852, Aug 1998.

[3] B. E. Kane, G. R. Facer, A. S. Dzurak, N. E. Lumpkin, R. G. Clark, L. N. Pfeiffer, and K. W. West. Quantized conductance in quantum wires with gate-controlled width and electron density. *Appl. Phys. Lett.*, 72(26):3506–3508, Jun 1998.

[4] B. J. van Wees, H. van Houten, C. W. J. Beenakker, J. G. Williamson, L. P. Kouwenhoven, D. van der Marel, and C. T. Foxon. Quantized conductance of point contacts in a two-dimensional electron gas. *Phys. Rev. Lett.*, 60(9):848–850, Feb 1988.

[5] D. A. Wharam, T. J. Thornton, R. Newbury, M. Pepper, H. Ahmed, J. E. F. Frost, D. G. Hasko, D. C. Peacock, D. A. Ritchie, and G. A. C. Jones. One–dimensional transport and the quantisation of the ballistic resistance. *J. Phys. C*, 21:L209–L214, Jan 1988.

[6] A. Kawabata. Theory of balistic transport through a constriction-quantization of conductance. *J. Phys. Soc. Jpn.*, 58(2):372–375, Dec 1989.

[7] D. J. Reilly, G. R. Facer, A. S. Dzurak, B. E. Kane, R. G. Clark, P. J. Stiles, R. G. Clark, A. R. Hamilton, J. L. O'Brien, N. E. Lumpkin, L. N. Pfeiffer, and K. W. West. Many-body spin-related phenomena in ultra low-disorder quantum wires. *Phys. Rev. B*, 63(12):121311, Mar 2001.

[8] B. J. van Wees, L. P. Kouwenhoven, E. M. M. Willems, C. J. P. M. Harmans, J. E. Mooij, H. van Houten, C. W. J. Beenakker, J. G. Williamson,

and C. T. Foxon. Quantum ballistic and adiabatic electron transport studied with quantum point contacts. *Phys. Rev. B*, 43(15):12431–12453, May 1991.

[9] A. Kristensen, Jensenm J. Bo, M. Zaffalon, C. B. Sørensen, S. M. Reimann, P. E. Lindelof, M. Michel, and A. Forchel. Conductance quantization above 30 k in gaalas shallow-etched quantum point contacts smoothly joined to the background 2deg. *J. Appl. Phys.*, 83(1):607–609, Jan 1998.

[10] R. D. Tscheuschner and A. D. Wieck. Quantum ballistic transport in in-plane-gate transistors showing onset of a novel ferromagnetic phase transition. *Superlattices and Micro.*, 20(4):616, May 1996.

[11] A. Gold and L. Calmels. Valley- and spin-occupancy instability in the quasi-one-dimensional electron gas. *Philos. Mag. Lett.*, 74(1):33, Mar 1996.

[12] A. Ramšak and J. H. Jefferson. Shot noise reduction in quantum wires with the 0.7 structure. *Physical Review B (Condensed Matter and Materials Physics)*, 71(16):161311, 2005.

[13] K. F. Berggren and I. I. Yakimenko. Effects of exchange and electron correlation on conductance and nanomagnetism in ballistic semiconductor quantum point contacts. *Phys. Rev. B*, 66(8):085323, Aug 2002.

[14] Anton A. Starikov, Irina I. Yakimenko, and Karl-Fredrik Berggren. Scenario for the 0.7-conductance anomaly in quantum point contacts. *Phys. Rev. B*, 67(23):235319, Jun 2003.

[15] P. Havu, M. J. Puska, R. M. Nieminen, and V. Havu. Electron transport through quantum wires and point contacts. *Phys. Rev. B*, 70(23):233308, Dec 2004.

[16] F. Malet, M. Pi, M. Barranco, and E. Lipparini. Ground state structure and conductivity of quantum wires of infinite length and finite width. *Physical Review B (Condensed Matter and Materials Physics)*, 72(20):205326, 2005.

[17] S. M. Cronenwett, H. J. Lynch, D. Goldhaber-Gordon, L. P. Kouwenhoven, C. M. Marcus, K. Hirose, N. S. Wingreen, and V. Umansky. Low-temperature fate of the 0.7 structure in a point contact: A kondo-like correlated state in an open system. *Phys. Rev. Lett.*, 88(22):226805, May 2002.

[18] Yigal Meir, Kenji Hirose, and Ned S. Wingreen. Kondo model for the “0.7 anomaly” in transport through a quantum point contact. *Phys. Rev. Lett.*, 89(19):196802, Oct 2002.

[19] Kenji Hirose, Yigal Meir, and Ned S. Wingreen. Local moment formation in quantum point contacts. *Phys. Rev. Lett.*, 90(2):026804, Jan 2003.

[20] K. A. Matveev. Conductance of a quantum wire at low electron density. *Phys. Rev. B*, 70(24):245319, Dec 2004.

[21] W. Apel and T. M. Rice. Combined effect of disorder and interaction on the conductance of a one-dimensional fermion system. *Phys. Rev. B*, 26(12):7063–7065, Dec 1982.

[22] C. L. Kane and Matthew P. A. Fisher. Transmission through barriers and resonant tunneling in an interacting one-dimensional electron gas. *Phys. Rev. B*, 46(23):15233–15262, Dec 1992.

[23] Masao Ogata and Hidetoshi Fukuyama. Collapse of quantized conductance in a dirty tomonaga-luttinger liquid. *Phys. Rev. Lett.*, 73(3):468–471, Jul 1994.

[24] Dmitrii L. Maslov and Michael Stone. Landauer conductance of luttinger liquids with leads. *Phys. Rev. B*, 52(8):R5539–R5542, Aug 1995.

[25] I. Safi and H. J. Schulz. Transport in an inhomogeneous interacting one-dimensional system. *Phys. Rev. B*, 52(24):R17040–R17043, Dec 1995.

[26] V. V. Ponomarenko. Renormalization of the one-dimensional conductance in the luttinger-liquid model. *Phys. Rev. B*, 52(12):R8666–R8667, Sep 1995.

[27] A. Kawabata. On the renormalization of conductance in tomonaga-luttinger liquid. *J. Phys. Soc. Jpn.*, 65(1):30, Jan 1995.

[28] Yuval Oreg and Alexander M. Finkel'stein. dc transport in quantum wires. *Phys. Rev. B*, 54(20):R14265–R14268, Nov 1996.

[29] C. L. Kane and Matthew P. A. Fisher. Transport in a one-channel luttinger liquid. *Phys. Rev. Lett.*, 68(8):1220–1223, Feb 1992.

[30] Akira Furusaki and Naoto Nagaosa. Resonant tunneling in a luttinger liquid. *Phys. Rev. B*, 47(7):3827–3831, Feb 1993.

[31] Michele Casula, Sandro Sorella, and Gaetano Senatore. Ground state properties of the one-dimensional coulomb gas using the lattice regularized diffusion monte carlo method. *Physical Review B*, 74(24):245427, 2006.

[32] Elliott Lieb and Daniel Mattis. Theory of ferromagnetism and the ordering of electronic energy levels. *Phys. Rev.*, 125(1):164–172, Jan 1962.

[33] Silvio Vitiello, Karl Runge, and M. H. Kalos. Variational calculations for solid and liquid *he*4 with a “shadow” wave function. *Phys. Rev. Lett.*, 60(19):1970–1972, May 1988.

[34] S. A. Vitiello, K. J. Runge, G. V. Chester, and M. H. Kalos. Shadow wave-function variational calculations of crystalline and liquid phases of *he*4. *Phys. Rev. B*, 42(1):228–239, Jul 1990.

[35] F. Pederiva, S. A. Vitiello, K. Gernoth, S. Fantoni, and L. Reatto. Shadow wave function for liquid and solid *he*3. *Phys. Rev. B*, 53(22):15129–15135, Jun 1996.

[36] F. Pederiva, A. Ferrante, S. Fantoni, and L. Reatto. Quantum theory of solid-liquid coexistence and interface in *he*4. *Phys. Rev. Lett.*, 72(16):2589–2592, Apr 1994.

[37] Francesco Operetto and Francesco Pederiva. Effect of vacancies on the structure of solid molecular parahydrogen studied with variational monte carlo simulations. *Phys. Rev. B*, 75:064201, 2007.

[38] S. A. Vitiello, L. Reatto, G. V. Chester, and M. H. Kalos. Vortex line in superfluid *he*4: A variational monte carlo calculation. *Phys. Rev. B*, 54(2):1205–1212, Jul 1996.

[39] M. H. Kalos and P. A. Whitlock. *Monte Carlo Methods.* A Wiley-Interscience Publication, 1986.

[40] Equation of state calculations by fast computing machines. *J. Chem. Phys.*, 21(6):1087, Jun 1953.

[41] Foulkes W. M. C., Mitas L., Needs R. J., and Rajagopal G. Quantum monte carlo simulations of solid. *Rewiews of Modern Physics*, 73(1):33, Jan 2001.

[42] P. J. Reynolds, D. M. Ceperley, B. J. Alder, and W. A. Lester. Fixed-node quantum monte carlo for molecules. *J. Chem. Phys.*, 77(1):5593, Dec 1982.

[43] Karl J. Runge. Quantum monte carlo calculation of the long-range order in the heisenberg antiferromagnet. *Phys. Rev. B*, 45(13):7229–7236, Apr 1992.

[44] J. Casulleras and J. Boronat. Unbiased estimators in quantum monte carlo methods: Application to liquid *he*4. *Phys. Rev. B*, 52(5):3654–3661, Aug 1995.

[45] A. D. Guclu, Gun Sang Jeon, C. J. Umrigar, and J. K. Jain. Quantum monte carlo study of composite fermions in quantum dots: The effect of landau-level mixing. *Physical Review B (Condensed Matter and Materials Physics)*, 72(20):205327, 2005.

[46] C. J. Umrigar, Julien Toulouse, Claudia Filippi, S. Sorella, and R. G. Hennig. Alleviation of the fermion-sign problem by optimization of many-body wave functions. *Physical Review Letters*, 98(11):110201, 2007.

[47] Julien Toulouse and C. J. Umrigar. Optimization of quantum monte carlo wave functions by energy minimization. *J. Phys. C*, 126:084102, 2007.

[48] M. P. Allen and D. J. Tildesley. *Computer Simulation of Liquids.* Oxford University Press, 1987.

[49] D. E. Parry. *The Electrostatic Potential in the Surface Region of an Ionic Crystal*, volume 49 of *Surface Science*, pages 433–440. North-Holland Publishing Company, 1975.

[50] Yuqing Xiao, M. F. Thorpe, and J. B. Parkinson. Two-dimensional discrete coulomb alloy. *Phys. Rev. B*, 59(1):277–285, Jan 1999.

[51] A. Grzybowski, E. Gwóźdź, and A. Bródka. Ewald summation of electrostatic interactions in molecular dynamics of a three-dimensional system with periodicity in two directions. *Phys. Rev. B*, 61(10):6706–6712, Mar 2000.

[52] William H. Press, William T. Vetterling, Saul A. Teukolsky, and Brian P. Flannery. *Numerical recipes in C++.* Second edition. Cambrige University Press, 2002.

[53] C. J. Umrigar, K. G. Wilson, and J. W. Wilkins. Optimized trial wave functions for quantum monte carlo calculations. *Phys. Rev. Lett.*, 60(17):1719–1722, Apr 1988.

[54] C.J. Umrigar, K.G. Wilson, and J.W. Wilkins. *Computer Simulation Studies in Condensed Matter Physics: Recent Developments.* Springer-Verlag, 1988.

[55] C. Filipp and Umrigar. Multiconfiguration wave functios for quantum monte carlo calculations orf first-row diatomic molecules. *J. Chem. Phys.*, 105(1), Jul 1996.

[56] C. J. Umrigar. Accelerated metropolis method. *Phys. Rev. Lett.*, 71(3):408–411, Jul 1993.

[57] C. J. Umrigar. *Variational Monte Carlo Basics and Applications to Atoms and Molecules.* Kluwer Academic Publishers, 1999.

[58] C. J. Umrigar, M.P. Nightingale, and K.J. Runge. A diffusion monte carlo algorithm with very small time-step errors. *J. Chem. Phys.*, 99(4):6, Aug 1993.

[59] K. Karkkainen, M. Koskinen, S. M. Reimann, and M. Manninen. Magnetism in one-dimensional quantum dot arrays. *Physical Review B (Condensed Matter and Materials Physics)*, 72(16):165324, 2005.

[60] B. Tanatar and D. M. Ceperley. Ground state of the two-dimensional electron gas. *Phys. Rev. B*, 39(8):5005–5016, Mar 1989.

[61] L. Dandrea and F. Pederiva. A shadow wave function for the two–dimensional electron gas. In *Proceedings of the LT 24 Conference*, AIP Conference Proceedings series, 2006.

[62] F. Pederiva. page 141, 1998. Condensed Matter Theories.

[63] R. A. Aziz, V. P. S. Nain, J. S. Carley, W. L. Taylor, and G. T. McConville. *J. Chem. Phys.*, 70:4330, 1970.

[64] Saverio Moroni, Stefano Fantoni, and Gaetano Senatore. Euler monte carlo calculations for liquid $he4$ and $he3$. *Phys. Rev. B*, 52(18):13547–13558, Nov 1995.

[65] C. Lin, F. H. Zong, and D. M. Ceperley. Twist-averaged boundary conditions in continuum quantum monte carlo algorithms. *Phys. Rev. E*, 64(1):016702, Jun 2001.

[66] Saverio Moroni, Francesco Pederiva, Stefano Fantoni, and Massimo Boninsegni. Equation of state of solid $3he$. *Phys. Rev. Lett.*, 84(12):2650–2653, Mar 2000.

[67] S. M. Heald, D. R. Baer, and R. O. Simmons. Thermal vacancies in solid 3he. *Phys. Rev. B*, 30:2531, 1984.

[68] V. N. Grigor'ev and Ye. O. Vekhov. The universality of energy spectrum of phonon and vacancy excitations in solid helium. *J. Low Temp. Phys.*, 149:41, 2007.